Universidade de Aveiro
2018

Departamento de Engenharia de Materiais e Cerâmica

FREDERICO PEDRO CARREIRA

DESENVOLVIMENTO DE TERMOELÉTRICOS POR LASER PARA CONVERSÃO DE ENERGIA A ALTAS TEMPERATURAS

Universidade de Aveiro
2018
Departamento de Engenharia de Materiais e Cerâmica

FREDERICO PEDRO CARREIRA

DESENVOLVIMENTO DE TERMOELÉTRICOS POR LASER PARA CONVERSÃO DE ENERGIA A ALTAS TEMPERATURAS

DEVELOPMENT OF THERMOELECTRICS FOR HIGH TEMPERATURE ENERGY CONVERSION BY LASER PROCESSING

Dissertação apresentada à Universidade de Aveiro para cumprimento dos requisitos necessários à obtenção do grau de Mestre em Engenharia de Materiais, realizada sob a orientação científica do Doutor Andrei Kavaleuski, Equiparado a Investigador Principal do Departamento de Engenharia de Materiais e Cerâmica e do Doutor Nuno Ferreira, Estagiário de Pós-Doutoramento do Departamento de Física.

o juri

presidente

Professor Doutor Joaquim Manuel Vieira
Professor Catedrático do Departamento de Engenharia de Materiais e Cerâmica da Universidade de Aveiro

vogais

Doutor Duncan Paul Fagg
Equiparado a Investigador Principal do Departamento de Engenharia Mecânica da Universidade de Aveiro

(arguente)

Doutor Andrei Kavaleuski
Equiparado a Investigador Principal do Departamento de Engenharia de Materiais e Cerâmica da Universidade de Aveiro

(orientador)

agradecimentos

Agradeço em especial aos meus orientadores, Doutor Andrei Kavaleuski e Doutor Nuno Ferreira por toda ajuda, apoio, disponibilidade e conhecimento transmitido para a concretização deste trabalho. Ao corpo técnico do DEMaC e do DFis pela colaboração e pelas condições de trabalho proporcionadas bem como aos meus colegas de laboratório. Aos meus pais e irmãos pela motivação e por estarem sempre a meu lado. Agradeço a todos os meus amigos com quem partilhei esta caminhada e que estiveram presentes nesta etapa final. Agradeço também a todos os meus amigos e conhecidos que comigo se cruzaram em meio académico ou não ao longo destes anos. O trabalho desta tese foi realizado no âmbito do projeto REMOTE POCI-01-0145-FEDER-031875, suportado pelos orçamentos do Programa Operacional POCI, na sua componente FEDER, e da Fundação para a Ciência e a Tecnologia, na sua componente de Orçamento de Estado.

palavras-chave

Materiais termelétricos, processamento por Fusão de Zona por Laser, eletrocerâmica, manganite de cálcio, substituição por Pr, praseodímio, coeficiente de Seebeck, propriedades eléctricas, performance termoeléctrica.

resumo

Neste trabalho foi processada por fusão de zona por laser (LFZ – Laser Floating Zone) a manganite de cálcio, em que o cálcio foi substituído por um dador: $Ca_{1-x}Pr_xMnO_3$ (x=0.03, 0.06, 0.1). Este sistema é um promissor semicondutor do tipo *n* para aplicação termoelétrica a altas temperaturas. Foram crescidas fibras com velocidades de 200, 100 e 25 mm h^{-1} em atmosferas de ar, vácuo e Árgon. As condições de processamento foram primeiro otimizadas com testes preliminares e sua caracterização estrutural e microestrutural. As condições de equilíbrio impostas pelo processamento da LFZ induziram amostras polifásicas nas fibras cerâmicas de $(Ca,Pr)MnO_{3-\delta}$, em alguns casos acompanhadas de um pronunciado crescimento de dendrites, muito típicos desta técnica. Nas baixas velocidades de crescimento (25 mm h^{-1}) verificou-se que favoreceram o aparecimento da fase do tipo perovskite, contudo as fibras eram muito frágeis. Foi estudado o efeito do tratamento térmico às amostras crescidas a 100 e 25 mm h^{-1} para a alteração para as fases desejadas neste material. Foi observado que estes tratamentos térmicos originavam maior homogeneidade na composição das fases, e morfologia das fibras melhorando o comportamento termoelétrico. A condutividade elétrica foi melhorada com o aumento da incorporação de praseodímio, por consequência observou-se o decréscimo no coeficiente de Seebeck. No fator de potência foi obtido um valor máximo de 303 μW m^{-1} k^{-2} a 1120 K para amostra com x = 0.06 crescida a 100 mm h^{-1}, e tratada termicamente em ar, sendo os valores comparáveis ou mesmo superior aos até agora reportados na literatura, processados pela via convencional. Testes isotérmicos da condutividade elétrica e coeficiente de Seebeck em temperaturas elevadas mostraram aumento da capacidade termoelétrica com o tempo em fibras crescidas sem tratamento térmico. Os resultados demonstraram que a técnica de LFZ pode ser usada como processamento de materiais termoelétricos, se otimizados os parâmetros de crescimento e condições de reequilíbrio das fases.

keywords

Thermoelectric materials, laser floating zone processing, electroceramics, calcium manganite, Pr donor-substituted, rare earth, Seebeck coefficient, electrical properties, thermoelectric performance.

abstract

Laser-processed donor-substituted calcium manganite $Ca_{1-x}Pr_xMnO_3$ (x=0.03, 0.06, 0.1) was accessed as a promising *n*-type thermoelectric material for high-temperature applications. Rod-like fibres were grown by laser floating zone technique (LFZ) at pulling rates of 200, 100 and 25 mm h^{-1} in various gas atmospheres, including air, vacuum and argon. Laser processing conditions were firstly optimized by preliminary experiments and corresponding structural and microstructural characterization. Strongly non-equilibrium conditions imposed by LFZ in all cases resulted in non-single phase $(Ca,Pr)MnO_{3-\delta}$ ceramic fibres, in several cases with possessing dendritic structures specific for LFZ. Slow pulling rate of 25 mm h^{-1} favoured perovskite single-phase composition but resulted in very fragile fibres. Thermal post-treatment was attempted to improve the composition regarding content of the thermoelectric perovskite-type phase and mechanical strength of the samples. This approach was successful, leading to homogeneous phase composition, fibre morphology and significantly higher thermoelectric performance. Electrical conductivity was enhanced with the praseodymium content, in contrast to lowering the Seebeck coefficient. A maximum power factor value of 303 μW m^{-1} K^{-2} at 1120 K was observed for the fibre with x=0.06 grown at 100 mm h^{-1} and thermally treated in air, being comparable or higher compared to those so far reported in the literature, processed by conventional routes. Isothermal tests of electrical conductivity and Seebeck coefficient under elevated temperatures were performed and revealed an increase in thermoelectric performance for as-grown fibres. The results have demonstrated that LFZ is a suitable technique for processing of thermoelectric perovskite-type manganites, if optimized control over growth parameters and re-equilibration conditions is imposed.

GENERAL INDEX

I. FIGURE INDEX

II. TABLE INDEX

III. LIST OF ABBREVIATIONS & SYMBOLS

A – Cross section area

a.u. – Arbitrary units

Ar – Argon gas

ACS – American chemical society

CAS – Chemical abstracts service

CS – Soft chemistry

C_v – Heat capacity

CVD – Chemical vapour deposition

DC – Direct current

DOS – Density of charges

EDS – Energy dispersive spectroscopy

LFZ – Laser floating zone

MNF – Mean free path

NASA – National aeronautics and space administration

Nd:YAG – Neodymium-doped yttrium aluminium garnet

$p(O_2)$ – Oxygen partial pressure

PF – Power factor

PVA – Polyvinyl alcohol

RT – Room temperature

RTGG - Reactive templated grain growth

S – Seebeck coefficient

SEM – Scanning electron microscopy

SPS – Spark plasma sintering

TE – Thermoelectric

T_c – Temperature of the cold end of the material

T_h – Temperature of the hot end of the material

V – Volume

VFA – Void forming agent

XRD – X-ray diffraction

ZT – Figure of merit

U – Potential difference

α – Thermopower

β – Thomson effect

ΔT – Temperature difference

μ – Energy conversion efficiency

Π – Peltier coefficient

ρ – Electrical resistivity

σ – Electrical conductivity

CHAPTER 1

INTRODUCTION

1 INTRODUCTION

Human need for energy has been on the rise since the industrial revolution in the 18th and 19th centuries. Mechanised manufacturing processes were evolved during this period and these were demanding high energy. Development in the field of technology further fuelled the demand for energy. During this period the need for energy was continuously increasing and it was realised that the fossil fuels are not a permanent energy source. To support the technological development in the field of science and considering the rate at which the fossil fuels were exploited, many new technologies were evolved for alternate energy source (Date, 2014). Energy production, conservation and management is not effective today. The statistical results show that around 60% of primary energy is lost worldwide, mostly in the form of heat (Zhang, 2015b). This waste heat is originated from various processes (e.g. combustion, chemical reactions, nuclear decay) and can be used as a source of power, when employing thermoelectric conversion (Sootsman, 2009). High performance thermoelectric (TE) materials directly and reversibly convert heat to electrical energy involving an environment-friendly energy technology, with the advantages of being scalable and reliable (Zhang, 2015b). Also, the absence of any moving parts makes thermoelectrics a promising technology for a wide range of applications. Such devices are not expected to replace primary power generation but can be used in hybrid concepts to improve total system efficiency. NASA was the first to implement the technology in a real application, back in 1961, to supply with electrical energy in space (Ewert, 1998). After that, many studies have been done in this field, but the attained efficiencies are still low. However, the technology has found its niches in the mainstream industry, and has been used for various applications such as heating in trains, powering wristwatches, cool diode lasers and several more (Date, 2014). Yet, thermoelectric technology is not able to compete with typical thermodynamic cycles (Vining, 2009). More recently though, from the 1990's, new approaches in the field thermoelectric materials brought back a lot of interest and research towards efficiencies near conventional heat engines. The manipulation at nano scales and the engineering of materials over processing conditions lead to an encouragement in the search for new ways to develop sustainable thermoelectric materials (Sootsman, 2009)(Date, 2014)(Koumoto, 2006)(Koumoto, 2013)(Wang, 2016)(Zhang, 2015).

1.1 THERMOELECTRIC MATERIALS

In order to contextualize the technology, an historical review of the concepts follows, with an overview of the thermoelectric principals, its challenges and the engineering that had raised with the technology. The material used for this work will be put in context with some state-of-the-art thermoelectric materials as well as the processing method.

1.1.1 Thermoelectric effects

In 1821 German physicist Thomas Johann Seebeck noticed that two dissimilar metals maintained at different temperatures cause a deflection on a compass needle (Seebeck, 1826). A schematic model of the thermoelectric effect based on Seebeck effect is presented in Fig. 1.1, showing different materials and junctions at different temperatures. At that time, this occurrence was explained by the magnetism induced by the temperature difference. However, later on Seebeck realised that there was a current flowing through the metals junction, which creates a magnetic field (Date, 2014). This phenomenon is characterized by the Seebeck coefficient (*S*) and it´s described as:

$$S = \frac{V}{\Delta T} \qquad \text{Eq. 1}$$

where V is the induced voltage and ΔT is the temperature difference between the cold and hot ends of the material. The gradient of temperatures drives the charge carriers in the material (electrons and/or holes) to diffuse from hot to cold sites, thus inducing a current (Zhang, 2015b). Because the materials are connected, a current flow through the circuit is maintained.

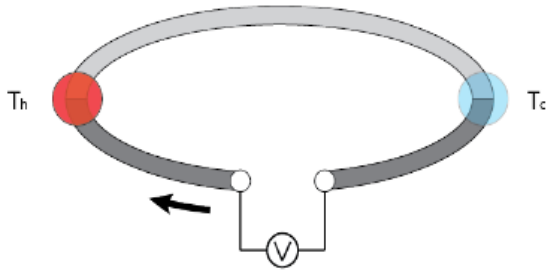

Figure 1.1 - Setup of Seebeck experiment. The scheme shows hot (T_h) and cold (T_c) spots where two dissimilar metals (in two shades of grey) are joined and the direction of the flowing current (Mazur, 2015).

One decade later, in 1834, French scientist Jean Charles Peltier (Bell, 2008) discovered the reversed Seebeck effect. He found out that, by inducing a current (I) in the circuit, consisting of two dissimilar metals, the junction is heated or cooled. As expressed in the following equation, Π, is the Peltier coefficient, Q_P is the heat produced or absorbed by the Peltier effect, and A and B represent two different materials:

$$Q_P = (\Pi_A - \Pi_B)\, I = \Pi_{AB}\, I = S_{AB}\, T\, I \qquad \text{Eq. 2}$$

At a given temperature, the heat generated is proportional to the current applied and to the Seebeck coefficient (S).

William Thompson (Thomson, 1853) in 1851 discovered the third thermoelectric effect with a relation between Seebeck and Peltier coefficients. In the Thompson effect, described by the equation below, the heat is absorbed or produced when current flows in a material with a temperature gradient:

$$Q_T = \beta\, I\, \frac{dT}{dx} \qquad \text{Eq. 3}$$

where β is the Thompson coefficient, I the electric current and $\frac{dT}{dx}$ the temperature gradient. Here, the relation shows a proportionality between heat and both the electric current and temperature gradient.

Since the values of Seebeck coefficient for known materials, possessing a reasonable electrical conductivity, are usually below 1 mV K^{-1}, the performance of simple thermoelectric couple (Fig. 1.1) is far from being sufficient for general applications. To increase the voltage output such couples must be connected electrically in series, thus connecting multiple couples like Fig. 1.1. A typical configuration of the thermoelectric module is presented in Fig. 1.2. The charge carriers (both electrons, $\boldsymbol{e^-}$ and holes, $\boldsymbol{h^+}$) tend to flow from hot to cold side, creating opposite charging. In this way, *n*- and *p*-type materials can be connected to generate a thermoelectric force. Actually, such configuration involves a number of challenges to be solved, including chemical and thermochemical expansion compatibility of the materials and similar performances.

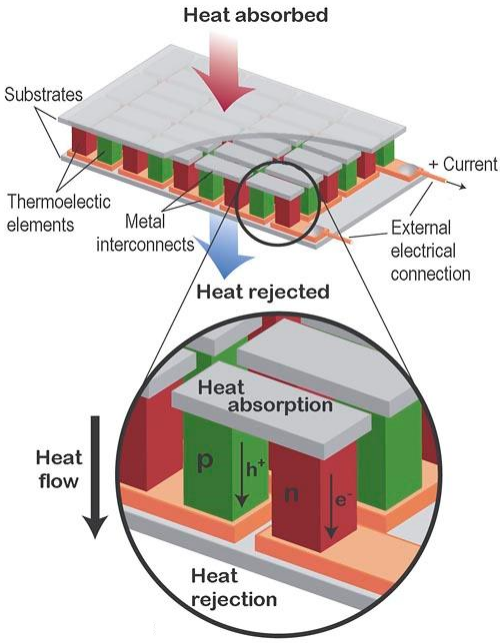

Figure 1.2 - Thermoelectric module for power generation. Operational thermoelectric device can be made of sets of couples (green and red thermoelectric elements) arranged in series, wired and covered by a ceramic substrate (Saidur, 2012).

1.1.2 Energy conversion efficiency

In 1949 Abram Fedorovich Ioffe developed a modern theory of thermoelectric materials and introduced an abbreviation (*ZT*), a dimensionless figure of merit used to evaluate the performance (Ohtaki, 2011):

$$ZT = \frac{S^2\sigma}{k}T \qquad \text{Eq. 4}$$

where *Z* describes the relationship between the three quantities determining the TE properties, *S* the Seebeck coefficient, σ is the electrical conductivity, *k* the thermal conductivity and *T* is the absolute temperature. Using this parameter, one may perform selection and predict the prospects of a material for thermoelectric applications.

For power generation, thermoelectric energy conversion is defined by combining Carnot efficiency $\frac{\Delta T}{T_h}$ and the figure of merit *ZT* as shown in following equation:

$$\eta = \frac{\Delta T}{T_h}\frac{\sqrt{1+ZT}-1}{\sqrt{1+ZT}+\frac{T_c}{T_h}} \qquad \text{Eq. 5}$$

where T_h and T_c are the temperatures of the hot and cold sides of a thermoelectric module and ΔT is the temperature difference. The term $(1+ZT)^{1/2}$ varies with the average temperature *T*.

This equation indicates that increasing efficiency requires both high *ZT* values and a large temperature gradient across the thermoelectric materials. Increasing *ZT* by a factor of 4, and depending on ΔT, the predicted efficiency can increase up to 30%, a highly attractive prospect. However, the efficiency of thermoelectric devices is not high enough to rival the Carnot efficiency (Sootsman, 2009) (Fergus, 2012).

Figure 3A illustrates a comparison by plotting heat sources (geothermal, solar, nuclear and coal) in combination with several thermal-to-electric conversion technologies (organic Rankine, Stirling, Brayton and steam Rankine) and the estimated efficiency of a thermoelectric converter. Plotted *ZT* lines are estimated by a simplified but optimistic method. It is notorious that existing, practical mechanical systems are far more efficient than thermoelectrics, and are more efficient than thermoelectrics are likely to become in the future. In all shown temperature range, thermoelectric system efficiency is below existing commercially available technology systems. Size, however, can favour thermoelectric technology. Figure 3B shows efficiency versus power generation for "heat engines" and thermoelectrics. Plotted curves represent again *ZT* values of efficiency for thermoelectrics and are illustrated in a schematic way (the numbers and shape of the curves are illustrative only). When scaled down in size, typical conversion systems become less efficient. This means there is a crossover efficiency point dictating that thermoelectric systems tend to be more efficient at small scale. This is valid also for *ZT* values under 1 (most of technology available today). So, there is an opportunity, where thermoelectrics can compete and have an impact on harvesting waste heat, namely, at relatively low power levels (Vining, 2009).

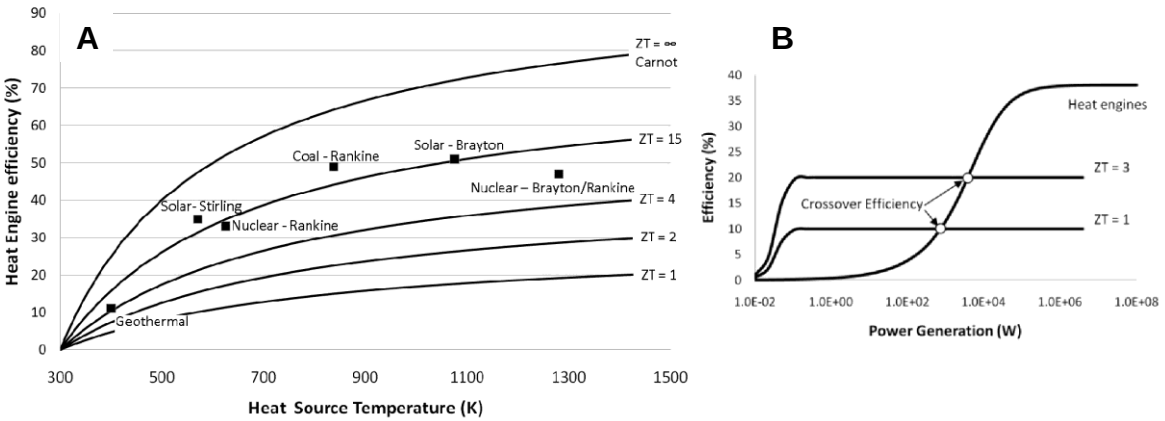

Figure 1.3 - Comparison on thermoelectric figure of merit *ZT* vs. efficiency of mechanical heat engines: heat source temperature dependence, A and power generation scale, B (Vining, 2009).

1.1.3 "Thermoelectric" challenges

For the best thermoelectric behaviour, high figure of merit (*ZT*) values are needed, thus implying a large Seebeck coefficient which ensures a good conversion for heat into electricity; high values of electrical conductivity to cover ohmic losses and Joule heat due to electrical resistivity and low thermal conductivity to minimize heat losses and maintain the thermal gradient. Point of concern is the correlation between these parameters as a function of charge carrier concentration. In fact, such coupling between the electrical (*S* and σ) and thermal (k) properties (Eq. 4), represent a main obstacle towards development of highly-efficient thermoelectrics for many years. Basic correlations describing this effect are presented below.

Based on thermodynamics considerations, the Seebeck coefficient can be described as (Alam, 2013):

$$S = \frac{8\pi^2 k_B^2}{3eh^2} m^* T \left(\frac{\pi}{3n}\right)^{\frac{3}{2}} \qquad \text{Eq. 6}$$

where k_B is the Boltzmann constant, *e* the electron charge, *h* the Plank´s constant, *m** the effective carrier mass, *T* the absolute temperature and *n* is the charge carrier concentration. At a given temperature, *S* depends on the carrier concentration, *n*.

The electrical conductivity can be represented as follows:

$$\sigma = \frac{1}{\rho} = ne\mu \qquad \text{Eq. 7}$$

where ρ is the electrical resistivity, *e* the electron charge and μ is the carrier mobility. This shows that higher carrier concentration leads to a higher conductivity, important for the thermoelectric performance. Thus, in terms of the charge carrier concentration, the requirements for increasing the electrical conductivity and Seebeck coefficient are, in fact, opposite (Eq. 4). Furthermore, the thermal conductivity can be represented as a sum of electronic and phonon contributions, namely:

$$k_{tot} = k_e + k_L \qquad \text{Eq. 8}$$

where k_e corresponds to the heat transported through the motion of charge carriers and k_L is the lattice counterpart of thermal conductivity, which corresponds to the heat transport by lattice vibrations (phonons).

The electronic contribution to the thermal transport is represented by Wiedemann-Franz´ law:

$$\kappa_e = LT\sigma \qquad \text{Eq.9}$$

where L (2.45×10^{-8} W Ω K^{-2}) is the Lorenz number, *T* the absolute temperature and *σ* the electrical conductivity (Chester, 1961). Thus, an increase in the charge carrier concentration enhancing the electrical conductivity also boosts the heat transport by charge carriers; both factors may result in almost negligible changes in the dimensionless figure of merit (Eq. 4). The contribution of the electronic counterpart of the thermal conductivity may vary depending on the type of the material. For instance, the total thermal conductivity of the insulators is basically governed by the propagations of phonons in the three space dimensions through the crystal structure, while in metallic materials the electronic thermal transport is predominant. Semiconductors lie somewhere at the borderline between insulators and metals, thus representing a best material of choice to tackle the challenge of coupling between the thermal and electrical properties.

The above considerations regarding thermoelectric coupling and the best materials can be further illustrated by plotting the thermoelectric parameters *vs.* charge carrier concentration, as shown in Fig. 1.4 (Wood, 1988). Following previous accounts between the Seebeck coefficient (*S*) and the electrical conductivity (*σ*) with the charge carriers (Eq. 6 and 7), the relationship can be illustrated as the two lines are presented with both parameters exhibiting opposite evolution. The quantity that relates with the electronic transport in a thermoelectric material is called power factor (PF) and is described as $S^2\sigma$. Therefore, PF relationship with the charge carriers has a maximum value where the best compromise is located. A large power factor means that a large voltage and a large current are generated.

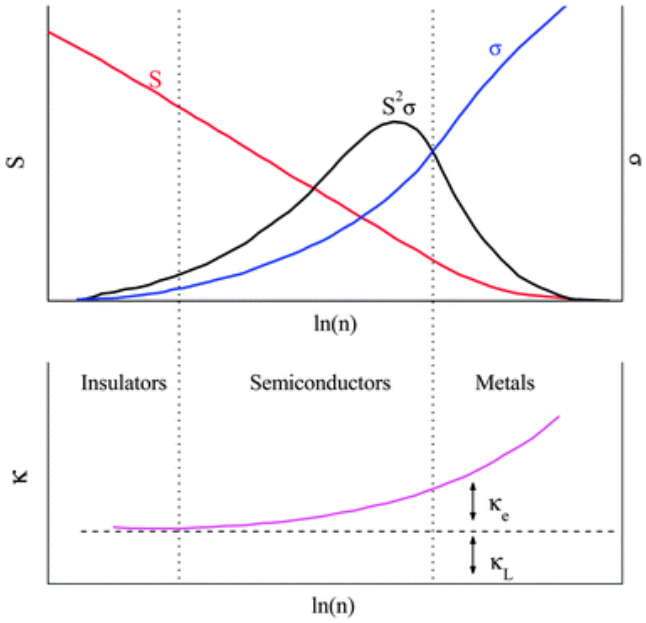

Figure 1.4 - Dependence of the thermoelectric parameters on the charge carrier concentration, plotted using a logarithmic scale.

Thermal conductivity (*k*) grows exponentially with carrier concentration: electronic contribution is significant only for semiconductors and metals, while the lattice contribution is independent on the charge carrier concentration (Billi, 2012). Thus, the properties of semiconducting materials represent a best compromise for seeking advanced thermoelectrics. In next session, approaches for enhancement of thermoelectric performance with individual fine-tuning are addressed.

1.1.4 Approaches to enhance the thermoelectric performance

Individual fine-tuning approaches have been done to envisage ways to increase the *ZT* in all three parameters: either the power factor is maximized, and/or thermal conductivity is minimized. Attempts to maximize power factor rely on the development of new classes of materials, exploration of nanoscale materials and the optimization of existing materials trough engineering of bands aiming to enhance the Seebeck coefficient.

In degenerate semiconductors, based on Eq. 6, a high S needs a high effective mass *m** or density-of-states (DOS) at given Fermi level (carrier concentration). Since $m^* = N_v^{2/3} m_b^*$, where N_v is the band degeneracy, and m_b^* is the band effective mass, there are two methods to increase the *m**, including increase the effective mass of the single pocket m_b^* or the band degeneracy (Pei, 2012)(Pei, 2011). However, a high m_b^* always leads to a low carrier mobility due to their inversion relation. Band engineering, increasing the factor N_v without changing much of m_b^*, can effectively solve the paradox between the DOS effective mass carrier mobility and has been treated as an efficient strategy to improve TE performance (Xi, 2016)(Naz, 2017)(Pei, 2012). Some excellent TE performance has been obtained, for example, by band engineering through distortion of the electronic DOS by doping Tl in PbTe, doubling *ZT* value (Heremans, 2012). The band structure mentioned above were caused by impurities.

Band degeneracy in its turn includes the orbital degeneracy (band degeneracy at one extrema point) and valley degeneracy (separate pockets at the same or similar energy). Highly degenerated bands indicate enhancement of m^* through increasing N_v, and therefore the Seebeck coefficient without significantly decreasing the electrical conductivity. By introducing multiple valley degeneracy, and band convergence by solid solutions *ZT* and PF values were improved (Pei, 2012)(W. Liu, 2012).

In most of the works, however, the dopants or compositions favourable to large degeneracies are found more or less by luck. So far, there is no systematic work that is able to provide clear criteria leading to the band convergence. Recently, Xi *et al*. work demonstrated the approach of rationally tuning crystal structures to design pseudocubic or cubic-like blocks in no-cubic diamond-like materials that can cause cubic-like degenerate valence band using a newly approach criteria (Zhang, 2014).

The minimization of thermal conductivity makes is way through the complex relationships between thermoelectric parameters. The lattice thermal conductivity k_L is the only parameter that is independent on carrier concentration. Therefore, reducing lattice thermal conductivity is an effective method to enhance thermoelectric performance. The lattice thermal conductivity is given by:

$$k_l = \frac{1}{3} C_v v l \qquad \text{Eq. 10}$$

where the heat capacity (C_v) and the phonon velocity (v) are constant, so the lattice thermal conductivity is governed by the phonon mean free pass (MFP) (l). One such route to lower the thermal conductivity is by increasing the lattice period (i.e. large unit cells parameters) thus providing short mean path lengths (by providing a longer more “energetic” path through the unit cell) for the heat carrying phonons. This effect was observed in ternary and quaternary Bi chalcogenides (Sootsman, 2009).

Inclusions/defects added to the material can equalize the MFP dimensions and effectively scatter the phonons. Acoustic phonons carry most of the heat in the material, and they have a spectrum of wavelengths and mean free paths distribution, including short, medium and long wavelength phonons, synergistically contributing to the total thermal conductivity (Lan, 2010). Therefore, all length-scale structures (solid solutions point defects, nano-scale precipitates and grain boundary), Fig. 1.5A, corresponding to the broad spectrum of heat-carrying phonons should be the main design principle for the enhancement of thermoelectric performance.

Distortion of unit cells which can be obtained by creating various types of defects in the lattice. The common types of defects that have significant effect on the thermal conductivity are structural imperfections, such as crystallite boundaries and dislocations.

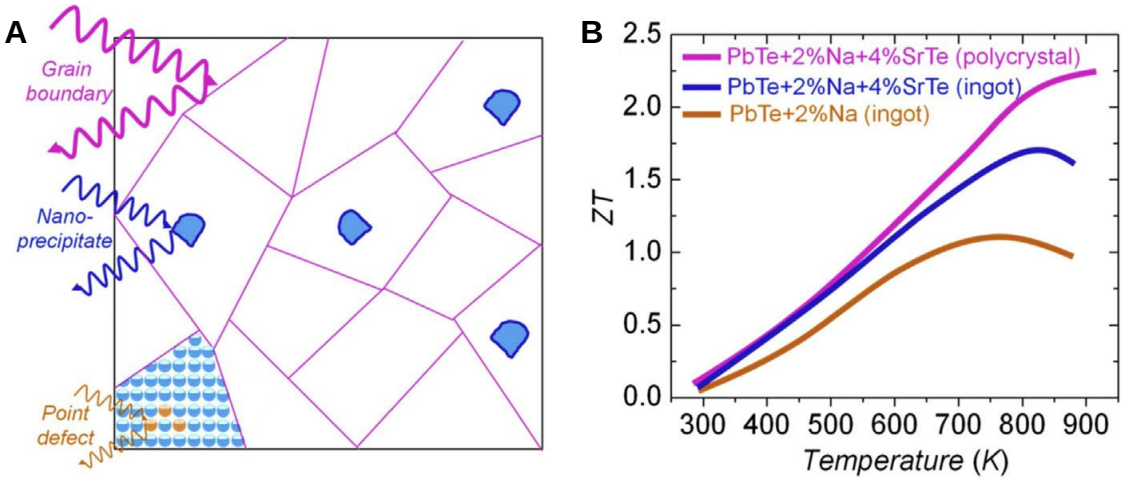

Figure 1.5 - All length scale structures to scatter short, medium and large wavelength phonons with solid solutions point defects, nano-scale precipitates and grain boundary, A and *ZT* values for the PbTe+2%Na ingot, PbTe+2%Na+4%SrTe ingot, and PbTe+2%Na+4%SrTe polycrystal, B (Zhang, 2015b).

Randomness in distribution of different kinds of atoms in the crystal, as the one occurring in alloys and solutions of impurities, also lowers the thermal conductivity. When creating defects by introducing foreign atoms one should be mindful of their valence, mass, size and interaction with the original atoms.

Foreign atoms of similar valence do not scatter free charge carriers but strongly scatters phonons due to difference in wavelengths of charge carriers and phonons. To maximize this effect, introduced atoms should be much larger and heavier than the original atoms. Concentration of the defects needed to lower thermal conductivity is temperature dependant and relatively large concentrations of lattice imperfections, will be required to produce significant effects at high temperatures where phonon scattering is the dominant mechanism. Adding vacancies is yet another effective method. Those tend to be more effective scattering the phonons, but they can act as electron acceptors and modify the electronic transport properties thus worsen thermoelectric performance.

Nano-inclusions can be obtained by several approaches, including embedded nano-inclusions, dispersing *in situ* partially oxidized nanoparticles in matrix and the endotaxial nano-precipitates. The last one comprehends the nucleation and growth of a second phase, which is required to have a low solubility in the solid state, but complete solubility on the liquid state (Zhao, 2014c). These new approaches and concepts for preparation of nanostructured materials typically diverge from the solid-state methods. An illustrative example for the thermal conductivity reduction is PbTe+2%Na+4%SrTe polycrystalline (Biswas, 2012) material, as shown in Fig 1.5B. The lattice thermal conductivity of PbTe was reduced by ~25% through Na doping; and further reduced by 55% through introducing of nanostructured SrTe; grain boundary contributes to a further significant reduction at high temperatures.

The overall thermal conductivity reached as low as ~0.5 W m^{-1} K^{-1} at 915 K. In terms of figure of merit *ZT*, optimal Na doping in p-type PbTe leaded to a *ZT* of ~1.1 at 775 K, which was further increased to ~1.7 at 800 K by introducing SrTe nano-precipitates, and eventually to ~2.2 at 915 K for PbTe+2%Na+4%SrTe polycrystalline through additional grain boundary scattering.

1.1.5 State-of-the-art thermoelectric materials

The Table 1 resumes some typical state-of-the-art bulk thermoelectric materials. At the beginning of 1990's the search for the new materials such as Skutterudites and Clathrates was notorious with *ZT* values reaching more than the unity. Furthermore, Zintl phases with large and complex unit cells including $Yb_{14}MnSb_{11}$ have been revealed to possess intrinsically low lattice conductivity due to high fraction of low velocity optical phonon modes. Alternatively, compounds with promising electrical transport properties but relatively large lattice thermal conductivity, such as half-Haulser, were studied. The *ZT* values of several materials, such as Bi_2Te_{3-} and PbTe-based ones (so called Chalcogenides), well exceed unity and are enough for commercial applications, but regardless of the environmental and materials cost. Nowadays with the emergence of cutting-edge technology and synergetic approaches exemplified in the previous section, make these bulk thermoelectric materials the ones leading the research frontier (Zhao, 2014b). Nanostructured, polycrystaline or even panoscopic materials have been under development recently, making these new concepts a part of a new generation of bulk thermoelectrics (Zhang, 2015b).

Table 1.1 – Typical thermoelectric materials and their performance.

	Material	Chemical composition / processing conditions	*ZT* value
Single phase	Skutterudites	$Ca_xCo_4Sb_{12}$	0.45 at 800 K (Puyet, 2004)
		$Ba_xCo_4Sb_{12}$	0.8 at 800 K (Dyck, 2002)
		$Ca_{0.18}Ni_{0.03}Co_{3.97}Sb_{12.4}$	1 at 800 K (Puyet, 2005)
		$Ba_{0.30}Ni_{0.05}Co_{3.95}Sb_{12}$	1.25 at 900 K (Tang, 2005)
	Clathrates	Type I - $Ba_8Ga_{16}Ge_{30}$	0.9 at 1000 K (Christensen, 2006)
		Type I - $Eu_8Ga_{16}Ge_{30}$	0.4 at 400 K (Bentien, 2005)
		Type III - $Ba_{24}Ga_{15}Ge_{100-15}$	1.25 at 943K (Kim, 2006)
		Type VIII - $Eu_8Ga_{16}Ge_{30}$	0.3 at 400 K (Bentien, 2004)
	half-Heulser	$Hf_{0.75}Zr_{0.25}NiSn_{0.975}Sb_{0.0025}$	0.78 at 1070 K (Yang, 2004)
		$(Zr_{0.5}Hf_{0.5})_{0.5}Ti_{0.5}NiSn_{1-y}Sb_y$	0.81 at 1025 K (Sakurada, 2005)
		$Zr_{0.5}Hf_{0.5}Ni_{0.8}Pd_{0.2}Sn_{0.99}Sb_{0.01}$	~1.4 at 700 K (Okamoto, 1991)
	β -Zn_4Sb_3		1.3 at 670 K (Caillat, 1997)
	The Zintl Phase $Yb_{14}MnSb_{11}$		~1 at 975–1275 K (Wood, 1984)
	Oxides	$NaCo_2O_4$	0.8 at 1000 K (Ohtaki, 2011)
		bismuth-doped $Ca_3Co_4O_9$	>1 at 1000 K (Sodeoka, 2000)
		$SrTiO_3$, heavily doped with Nb	0.37 at 1000 K (Koumoto, 2006)
		$(Al_{0.02}Zn_{0.98}O)$	0.3 at 1000 K (Ohtaki, 1996)
		Ca-doped $(ZnO)_3(In_2O_3)$, (RTGG method)	0.31 at 1053 K (Tani, 2004)
		$CaMn_{0.98}Nb_{0.02}O_3$ (SC method)	0.32 (Koumoto, 2013)
		BiCuSeO	1.4 at 923 K (Zhao, 2014a)
	SnSe		2.6 +/- 0.3 at 923 K (Zhao, 2014c)
Chalcogenide Compounds	Anisotropic Materials	Tl_9BiTe_6	1.2 at 500 K (Wölfing, 2001)
		Tl_2SnTe_5	1 at 500 K (Sharp, 1999)
		Bi_2Te_3 by hydrothermal synthesis	1.0 at 450 K (Zhao, 2005)
		Bi_2Te_3 by SPS	1.35 at 300 K (Tang, 2007)
		Bi_2Te_3 by direct current hot pressing	1.4 at 373 K (Poudel, 2008)
		$Cu_{2-x}Se$	1.5 at 1000 K (H. Liu, 2012)
		Cu_2Se	~1.6 at 972K (Yu, 2012)
		$Cu_{2-x}S$	1.7 at 1000 K (He, 2014)
		$Cu_2Se_{1-x}I_x$	2.3 at 400 K (Liu, 2013)
		β-Cu_2Se Al doped	2.62 at 1029 K (Zhong, 2014)
	Isotropic Materials	$AgSbTe_2$	1.3 at 720 K (Wood, 1988)
		PbTe:Tl system	1.5 at 773 K (Naz, 2017)
		$(AgSbTe_2)_{1-0.85}(GeTe)_{0.85}$	~1.5 at 750 K (Heremans, 2012)
Inhomogeneous Nanostructured Materials		PbS	1.1 at 923K (Okamoto, 1991)
		$NaPb_{18-x}SnMTe_{20}$ (M=Sb,Bi)	~1.3 at 670 K (Guéguen, 2009)
		$AgPb_mSn_nSbTe_{2+m+n}$	1.4 near 700 K (Zhou, 2008)
		$Ag_{0.8}Pb_{18+x}SbTe_{20}$	1.5 at 673 K (Okamoto, 1991)
Nanostructured polycrystalline Materials		SnSe (Na/K) – codoped	1.2 at 773 K (Ge, 2017)
		BiSbTe alloy	1.4 at 373K (Poudel, 2008)
		PbTe–SrTe–MnTe alloy	1.98 at 800 K (Luo, 2017)
		$PbTe_{0.98}Na_{0.02}$ - 4% SrTe by SPS	~2.2 at 900 K (Biswas, 2012)
		$PbTe_{0.98}Na_{0.02}$ - 8% SrTe	~2.5 at 923 K (Tan, 2016)
Panoscopic materials		PbSe	~1.6 at 923K (Zhao, 2014b)

1.1.6 Oxide thermoelectrics: $CaMnO_3$- based materials

Considering bulk thermoelectric materials (Table 1.1), oxides represent a very interesting option for high-temperature thermoelectric technology. Comparing with non-oxides, ZT values don't reach high numbers, but the point of concern is that, considering high-temperature applications, best known traditional TE materials can only be used under oxygen-free environment at relatively low temperatures, while also having high environmental impact due to presence of toxic elements. The fact that oxides allow high temperature operation is also important from the viewpoint of thermoelectric performance, since higher temperature difference results in higher Carnot efficiency of the conversion.

Seeing further improvements in durability, performance and decreased costs, these materials could play an important role in harvesting energy from waste heat (Fergus, 2012). The first studied oxide material with good thermoelectric properties was the $NaCo_2O_4$. This material with a layered structure has a large thermopower and metal-like conductivity due to CoO_2 layers, and underwent tremendous research (Sootsman, 2009)(Wang, 2016). Another form of Al-substituted ZnO was reported with the enhanced *ZT* of 0.4 at 773 K which was achieved by applying a void forming agent (VFA), such as nanoscale particles of carbon or organic polymer. An *n*-type composite phase, Ca substituted $(ZnO)_3(In_2O_3)$, fabricated by the reactive templated grain growth (RTGG) method was reported with *ZT*~0.31 at 1053 K (Sootsman, 2009).

Calcium manganite $CaMnO_3$ is one of the most studied perovskite type materials for thermoelectrical technology, due to high thermal and chemical stability in oxidizing atmosphere. The ABO_3 general formula couples the Ca atom as the A cation and Mn as the B-site transition metal, as shown in Fig. 1.6. The structure is normally orthorhombic and belongs to the *Pnma* space group. Such crystal structure allows an essentially low thermal conductivity. Electrical conductivity values according to literature, can reach up to 320 S cm^{-1} (Liu, 2013) and depend on the structure, degree of distortion and Mn oxidation state (Wang, 2010)(Zhang, 2011a).

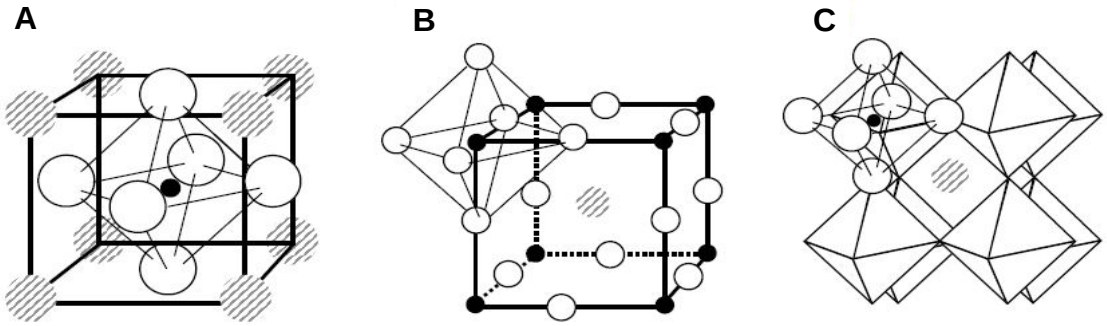

Figure 1.6 - Different representations of the cubic perovskite structure, where the A, B and O ions are represented by hatched, open and small black circles, respectively: (A) A cations at the corners, (B) A cations in the centre of the cell (C) ABO_3 perovskite structure in a perspective view where the corner-sharing BO_6 octahedra surrounds the A cation The edges of the BO_6 octahedra are indicated by thin lines (Billi, 2012).

To enhance TE properties, Seebeck coefficient values should be improved, as discussed above in the Chapter 1.1.4. The parameter relates to carrier concentrations, but also correlates with the crystal structure. Low lattice thermal conductivity contributes to higher figure-of merit of the material (Zhou, 2008). Despite high Seebeck coefficient, corresponding figure of merit *ZT* at high temperatures still remains low due to their relatively large resistivity. When some tri- or tetravalent elements are introduced into the $CaMnO_3$ lattices, the obtained electron-doped compounds exhibit lower resistivity and moderate Seebeck coefficients (Cong, 2004)(Xu, 2004)(Choi, 2011)(Kabir, 2014)(Kabir, 2015)(Zhang, 2011b)(Zhu, 2015). The thermoelectric

properties of the $CaMnO_3$ materials can be significantly improved with these substitutions. Therefore, perovskite-type manganites are expected to be promising *n*-type thermoelectric materials, and a large amount of research has been performed to enhance the thermoelectric properties using the substitution modification method.

Considering the sites where these elements are introduced, these studies can be categorized into three types (Mishra, 2017)(Zhang, 2015a). The first and second type method is to introduce substituents at the Mn or Ca sites, respectively, and the third one is based on simultaneous substitution of Mn and Ca (Wang, 2016). $CaMnO_3$ system itself is a poor *n*-type semiconductor. However, a lot of research to resolve this has been made especially with $CaMnO_3$ and $SrTiO_3$ systems through incorporation of elements. Recent work on this area is reviewed by Hongchao Wang *et.al* where perovskite type oxides are highlighted to be high-performance thermoelectric materials (Wang, 2016).

Single substitution on Mn site with Ru and Mo as $CaMn_{1-x}R_xO_3$ results in a low resistivity ($\rho < 0.03$ Ohm cm) and moderate Seebeck coefficient ($S > 100$ mV K^{-1}) at room temperature (Pi, 2003). In a $CaMn_{1-x}Nb_xO_3$ system, at high temperatures the manganite crystal structure changes from orthorhombic to cubic symmetry (Bocher, 2009). A promising approach for preparation of Nb-substituted calcium manganite is based on soft chemistry methods, like “chemie douce” (SC) synthesis, which leads to significant decrease in thermal conductivity, $k < 1$ W m^{-1} K^{-1}, and *ZT* of 0.32 (Bocher, 2008). Silver has been shown to increase the Seebeck coefficient while bismuth, either alone or co-doping with vanadium or niobium, has been shown to increase the electrical conductivity and the figure of merit (Fergus, 2012).

At the Ca site, the substitution of R^{3+} for Ca^{2+} causes an improvement of electrical conductivity of $CaMnO_3$ and sometimes induces a metal-insulator transition. According to the previous results, the thermal conductivity *k* is mainly dependent on the atomic weight of the R^{3+} ion. If some donors produce effectively positive defects in this perovskite, the charge valence of Mn^{4+} can be changed to Mn^{3+} in proportion to the amount of donor. As a result, this mixed valence between the Mn^{4+} and Mn^{3+} states can increase the charge carrier concentration (Koc, 1992). The heavier R^{3+} ion induces strong local vibrations in the system and suppresses the *k* in the $Ca_{0.9}R_{0.1}MnO_3$ system. For a $Ca_{0.9}R_{0.1}MnO_3$ system, the electron concentration, structural distortions, and the weight/size of substitution ions are related to the thermoelectric response (Michitaka, 1995)(Choi, 2011)(Wang, 2010)(Wang, 2009). The highest $ZT = 0.2$ was found in the $Ca_{0.9}Dy_{0.1}MnO_3$ and $Ca_{0.9}Yb_{0.1}MnO_3$ samples (Kabir, 2014). The high figure of merit is attributed to the relatively low resistivity and the low thermal conductivity among all $Ca_{0.9}R_{0.1}MnO_3$ samples. Additions of Bi is reported to result in the maximum power factor (4.67×10^{-4} W m^{-1} K^{-2}) achieved at 423 K for $Ca_{0.97}Bi_{0.03}MnO_3$ which is four times larger than that of the un doped $CaMnO_3$. The lowest thermal conductivity (1.4 W m^{-1} K^{-1}) was obtained at 973 K for the same composition ($x = 0.03$). The highest *ZT* reported so far for these systems is 0.3 in Nb-substituted $CaMnO_3$ (Koumoto, 2013). The authors did a comparative study by preparing samples using solid-state reactions (SSR) and soft chemistry method (SC). There was no obvious difference in Seebeck coefficient for the samples prepared by these different methods. However, the electrical conductivity of samples obtained by SC method was noticeably improved compared to the samples obtained by SSR method. This was attributed to the well-interconnected nano-sized grains formed in the samples prepared by SC method. Nanocrystallite grains induce phonon scattering centers, which explain lower thermal conductivity in SC samples. Therefore, SC method may be considered for the optimization of thermoelectric properties in $CaMnO_3$- based materials (Yin, 2017)(Kabir, 2015). Also, $Ca_{1-x}Pr_xMnO_3$ system has been studied recently showing promising high temperature thermoelectric behaviour (Choi, 2011). The thermoelectric performance was noticeably improved by Pr incorporation and the dimensionless figure of merit *ZT* for the $Ca_{0.92}Pr_{0.08}MnO_3$ compound was favourably optimized with the maximum value 0.16 at 873 K (Zhang, 2013), $Ca_{1-0.85}Pr_{0.15}MnO_{3-\delta}$ was 1.5×10^{-4} K^{-1} at T=1100 K (Cong, 2004).

The performances shown above suggest that praseodymium-substituted calcium manganite shows quite attractive *ZT*. Additional benefits may be foreseen from the redox sensitivity of praseodymium cations, namely, existence of Pr^{3+}/Pr^{4+} couples with expected effects

on electrical conductivity and Seebeck coefficient. Table 1.2 summarises *ZT* values for $CaMnO_3$ system over different processing ways. Among the materials processed by conventional routes, Pr substitution shows high *ZT* values and new processing methods are reported to increase the performance of such materials. Therefore, Pr-substituted calcium manganite was selected as a model system to study the relevant impacts of laser processing on the thermoelectric performance.

Table 1.2 – Thermoelectric properties and processing conditions for various CMO-based materials.

Composition	*ZT*	Processing conditions / Reference
$Ca_{0.96}Bi_{0.04}Mn_{0.96}Nb_{0.04}O_3$	0.1 at 873K	solid-state reaction method (Park, 2009)
$Ca_{0.95}La_{0.05}MnO_3$	0.19 at 1000K	solid-state reaction method (Mishra, 2017)
$Ca_{0.9}Dy_{0.1}MnO_3$ and $Ca_{0.9}Yb_{0.1}MnO_3$	0.2	solid-state reaction method (Wang, 2009)
$Ca_{0.97}Bi_{0.03}MnO_3$	~0.25 at 973 K	solid-state reaction method (Kabir, 2015)
$Ca_{0.9}Pr_{0.1}MnO_3$	0.28 at 1132 K	solid-state reaction method (Choi, 2011)
$Ca_{0.92}Pr_{0.08}MnO_3$	0.16 at 873 K	synthesized by citrate acid sol-gel reaction method (Zhang, 2013)
$CaMn_{0.98}Nb_{0.02}O_3$	0.32 at 1060 K	soft chemistry method (Koumoto, 2013)

1.2 LASER FLOATING ZONE TECHNIQUE

The Laser floating zone (LFZ) technique is reported in many works made in the field of optoelectronic and superconducting devices, and more recently in thermoelectric materials in a way to implement new structural characteristics, thus improving thermoelectric properties. Wide-band response and rapid synthesis by laser-induced (Zhang, 2009) and laser-melting (Kinemuchi, 2016) techniques were documented. Studies were made on Bi-based cobaltites (Sotelo, 2007), calcium-bismuth cobaltites and by electrically assisted laser floating zone (Ferreira, 2012), or strontium-bismuth cobaltites (Rasekh, 2015) and barium iron oxide (Ferreira, 2018a) using LFZ technique. It is a peculiar and matured way, inside non-conventional group of techniques used for crystal productions, presenting the advantages of growing materials with a high melting point (Ritzert, 1996). Moreover, being a crucible free process, it allows the production of high purity crystals and composite fibres, avoiding mechanical stress and contamination during the solidification process (Costa, 2005)(Ritzert, 1996).

1.2.1 Fundamentals and working method

Historically, LFZ processing method originates from improvements and refinement of techniques for crystal growth process using melts (Scheel, 2003). LFZ is based on applying a laser beam into the rod-like sample followed by melting, creating high thermal gradients and favouring high crystal alignment in materials (Neves, 2017)(Ritzert, 1996).

Fig. 1.7 shows a system to obtain a uniform molten zone through a mirrors setup for shape manipulation of the laser beam (Carvalho, 2013)(Costa, 2005). The laser must be sufficiently powerful to melt the material and maintain a stable condition of the molten zone. Several types of laser systems are been used to grow materials such as Nd:YAG, CO_2 and more recently diode lasers.

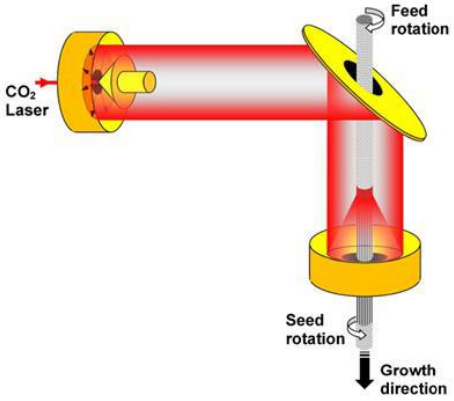

Figure 1.7 – Illustration of the laser floating zone mirrors setup (Carvalho, 2013).

The LFZ is basically a floating zone-like method where the heating element is a focused laser ring to create the molten zone.

The growing process starts with three main steps as Figure 1.8 illustrates:

a) The alignment of the feed and pedestal rods, both centralized in the optical axis of the laser beam with the formation of a molten zone on the bottom of the feed rod;
b) Unity of the molten tip of feed rod and the seed rod into a stable molten zone;
c) Pulling and rotation of the motors.

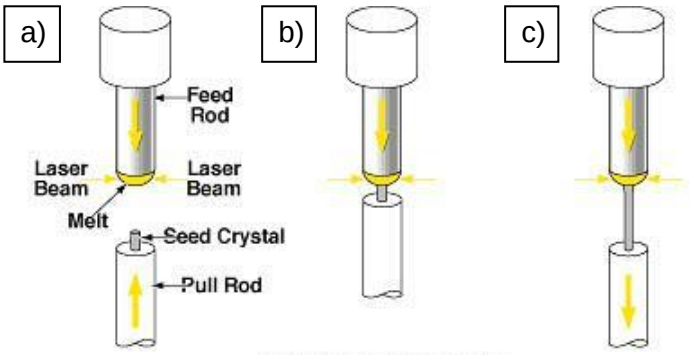

Figure 1.8 – Start of the seeding process illustrated by the three steps, a), b) and c). The vertical arrows represent the direction of the rods along the y-axis whereas the horizontal arrows represent the laser beam fixed in the y-axis (Ritzert, 1996).

To keep a constant volume, it is necessary to feed and pull at a fixed rate, since the crystal growth process is based in a mass conservation principle. The ratio between the speed of the feed and seed rods determine the diameter of the as-grown fibre. The growth speed and thermal conductivity of the material control the temperature gradient in the feed rod and crystal. If the thermal gradient is high due to the lower thermal conductivity, the crystal is instantaneously "quenched" as it leaves the molten zone, causing higher residual stresses (Ritzert, 1996).

A different effect occurs in the feed rod, as it decreases in temperature away from the melt, the powders change from highly sintered solids to loosely bonded powders, and eventually losing powders that are hot enough to drive off the binder material but not enough to be sintered.

In the LFZ process, the melt automatically adjusts the composition required to produce the appropriate steady state growth conditions. In some cases, fast growth can be advantageous to reduce the time in the molten zone, thus minimizing the vaporization process. However, in most cases slow pulling rates produce crystals with superior crystallinity. Obviously, there are optimum experimental conditions that give the best results for each specific system (Ritzert, 1996).

The principal growth parameters that play a key role during growth of single crystals are:

a) feed rod characteristics;
b) the growth rate;
c) the growth atmosphere and its pressure;
d) the temperature gradient;
e) the molten zone temperature;
f) the rotation rate.

The effect of these parameters becomes even more acute in the growth of materials which may have intrinsic properties such as high density, low surface tension or a complicated phase diagram (Ohtaki, 1995).

1.2.2 Applications

Crystal-growth technology including layer fabrication technology is of greatest importance for energy saving, for renewable energy, and for novel high technologies. In the last decades, the growth of amorphous and crystalline materials (single and polycrystals), have been successfully reported in several material science areas (Ritzert, 1996)(Ferreira, 2012). LFZ process has been developed into a quick extremely useful laboratory process to investigate amorphous, single-crystal and poly-crystal fibres that can be obtained by directional solidification from a melt induced by a beam laser incidence on the material. This method was already used to study phase transformation kinetics, diffusion phenomena and crystallization path of different systems.

The LFZ technique allows to produce oriented, small-diameter crystals that meet the requirements for high-temperature in today's advanced matrices, like high quality single crystals of a variety of oxides, eutectic structures and highly oriented polycrystalline materials.

Polycrystalline materials obtained by LFZ method can archive preferential crystals alignment due to strong thermal gradient at the solidification interface. Another advantage of the LFZ method is the high temperature reached due to the beam focus system. This technique allows the formation of high temperature metastable phases and crystallization of incongruent phases due to high thermal gradients generated at the melt/fibre interface which can reach 10^3 to 10^4°C cm^{-1}.

1.3 MOTIVATION AND MAIN GOALS

The motivation for this work originates from high attractiveness of oxide materials as cheap and eco-benign alternative to traditional thermoelectrics materials. A major challenge in developing highly-efficient thermoelectric materials is seeking a delicate balance between functional properties, namely, electrical and thermal conductivities and Seebeck coefficient. Laser floating zone processing is known for producing textured materials with tunable grain alignment and unique morphology, provided by very high-temperature treatments under strongly non-equilibrium conditions.

Up to now, the LFZ method was employed only for processing *p*-type layered cobaltite-type oxides and showed significant prospects for enhancing their performance. This work represents an attempt to apply this approach for promising *n*-type oxide thermoelectrics based on donor-substituted calcium manganite.

Another expectation behind is that, besides tailoring the thermoelectric properties, LFZ method allows to fabricate the samples almost in the final shape desired for thermoelectric module, which increases the technological relevance of the proposed work.

Finally, the aim of the project is the development of performing oxide thermoelectrics based on donor-substituted calcium manganite by unconventional processing employing laser floating zone method. The particular objectives include:

- to optimize LFZ processing conditions aiming dense and mechanically strong fibre-like samples, suitable for thermoelectric characterization;
- to perform detailed structural, microstructural and thermoelectric characterization;
- to understand the impacts of LFZ processing conditions on structural, microstructural and thermoelectric properties, and to elucidate main relevant mechanisms behind;
- to evaluate possible degradation of the thermoelectric performance under prospective operation conditions.
- to elaborate guidelines for designing highly-performing calcium manganite-based thermoelectrics by LFZ processing.

CHAPTER 2

EXPERIMENTAL PROCEDURE

2 EXPERIMENTAL PROCEDURE

This chapter gives an overview of the experimental part performed for this work, with description of the sample preparation, the laser floating zone technique and the characterization techniques used. A flowchart (Fig. 2.1) outlines the steps for a preview of the procedure.

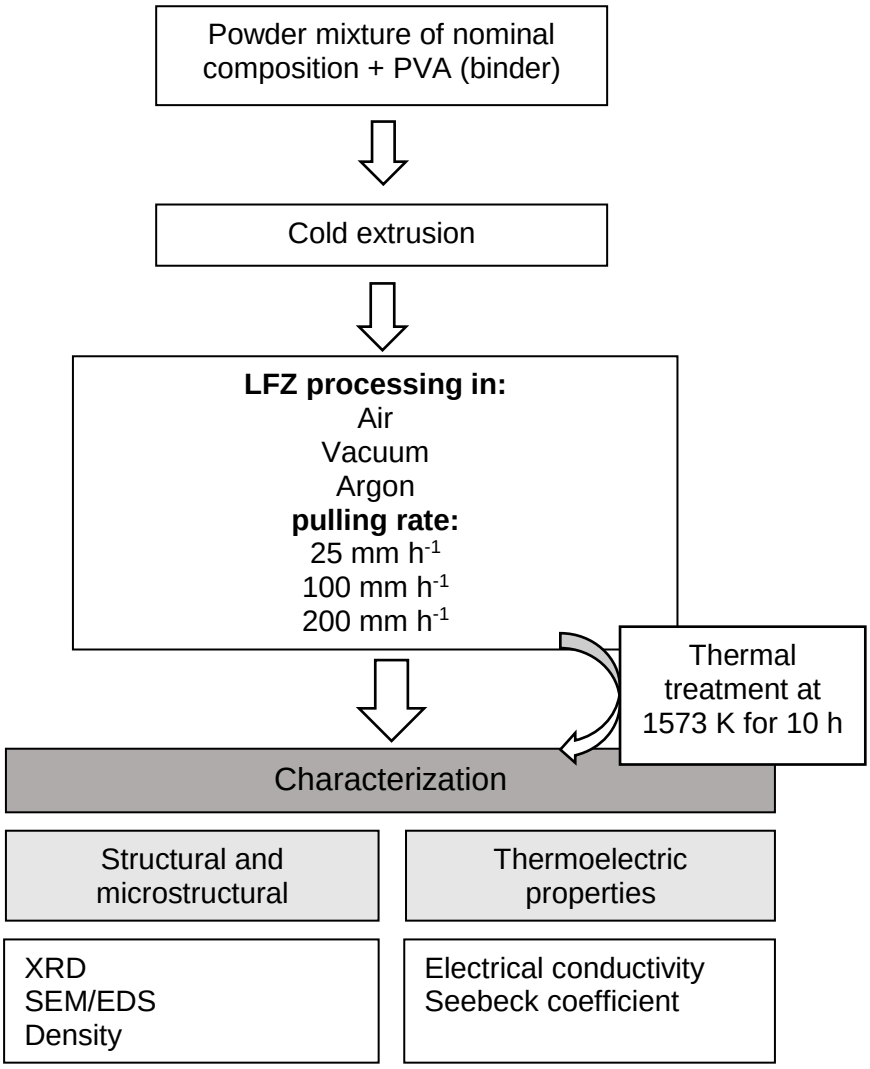

Figure 2.1 - Flowchart of the preparation and characterization procedures involved in the work.

The rod-like fibres, prepared by cold extrusion of the precursor powders in a stoichiometric mixture, were processed by laser floating zone method to produce highly-dense calcium manganite-based ceramic fibres. In order to assess the specific impacts of strongly-nonequilibrium LFZ conditions on the structural, microstructural and transport properties, as-grown fibres were subjected to posterior thermal treatment (1573 K for 10 hours). Further characterization included X-Ray diffraction analysis (XRD), scanning electron microscopy (SEM) coupled with energy dispersive spectroscopy (EDS), and measurements of density. The thermoelectric characterization included the measurements of the temperature dependence of the electrical conductivity and Seebeck coefficient. Isothermal thermoelectric measurements were performed at 1173 K to evaluate the stability issues under prospective operation conditions.

2.1 PREPARATION OF THE PRECURSOR FIBRES

Selected compositions range included praseodymium-substituted calcium manganite $Ca_{1-x}Pr_xMnO_3$, where x= 0,03; 0,06 and 0,10. As powder precursors, $CaCO_3$ (Alfa Aesar, ACS, 99.0%, CAS: 471-34-1), MnO_2 (Alfa Aesar, Manganese (IV) oxide 99.9%, CAS: 1313-13-9) and Pr_6O_{11} (Aldrich, Praseodimium (III, IV) oxide, 99.9%, CAS: 12037-29-5) were used. The powders were weighed in order to obtain the stoichiometric composition using a digital balance.

Before weighing, the praseodymium oxide was annealed at 1273 K for 2 hours with a 3 K/min cooling and heating rates to remove absorbed species and attain equilibrium composition of Pr_6O_{11}. All the powders were then mixed for 2-3 hours in a planetary mill using an Agate jar with steel casing (250 ml) (Fig. 2.2A), alumina balls and alcohol as a dispersant. After the alcohol evaporation done in an oven, the compositions were ready for extrusion.

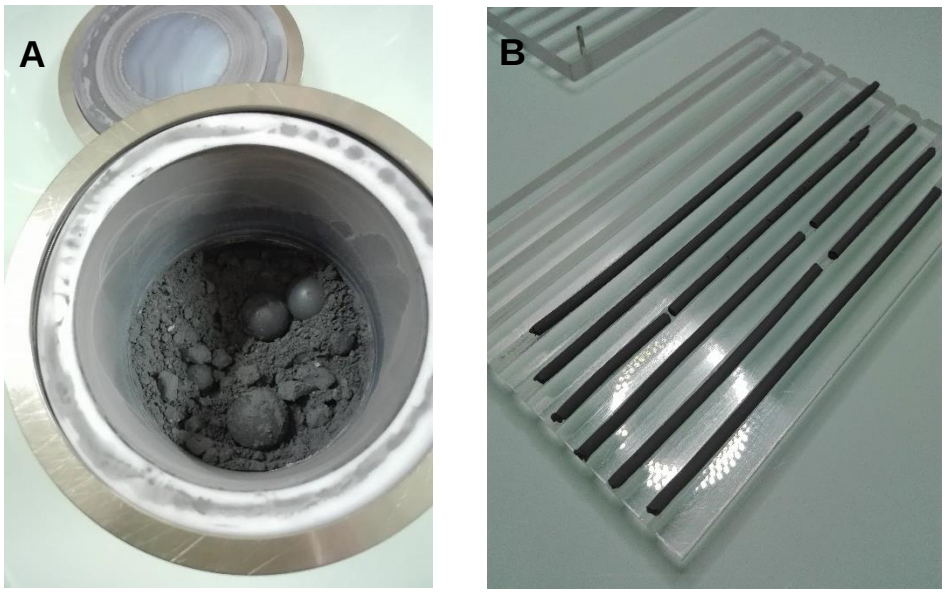

Figure 2.2 - Mixed powdered precursors, A and resulted extruded fibres, B.

The extrusion was performed using (polyvinyl alcohol PVA^- (Aldrich, 99.9%, pure), mixed with water (0.1 g ml^{-1}), as a binder. The amount of PVA added do the powder was optimized to provide a consistency desirable for extrusion. PVA is burned during laser processing. The extrusion resulted in rod-like fibres with 3 millimetres of diameter and length ~12 cm, suitable for further processing by LFZ, as shown in Figure. 2.2B. The material presents a cylindrical shape, to favour the chemical and thermal homogenization during the growth process. After extrusion, the material was dried in atmospheric conditions and used as rod-like precursor fibres for growth in the LFZ system.

2.2 LASER FLOATING ZONE PROCESSING

The LFZ equipment used in the present work included a laser system; a growth chamber with controlled atmosphere; a homemade monitoring system (laser parameters, pulling rate and rotation rate) with an image capture system. Figure 2.3 shows photographs of this LFZ setup, depicting the core elements of the system as well as a zoom of the chamber, where the growing process occurs. The system involves a 200W CO_2 continuous laser (Spectron SLC, λ = 10.6 μm) with a beam spot size of 4 mm (1).

A homemade program (2) based Labview® software (from National Instrument®), was used to monitoring and control, including the following hardware:

- Laser: on/off emission; power value (melting temperature), open/closed internal and external shutters;
- Motors: growth speed and direction, as well as homogeneity of the fibres by rotation of the feed and seed rods;
- Image capture and its control parameters (zoom, contrast and brightness) allow us to get a better visualization of the molten zone and mainly of the melt/solidification interfaces.

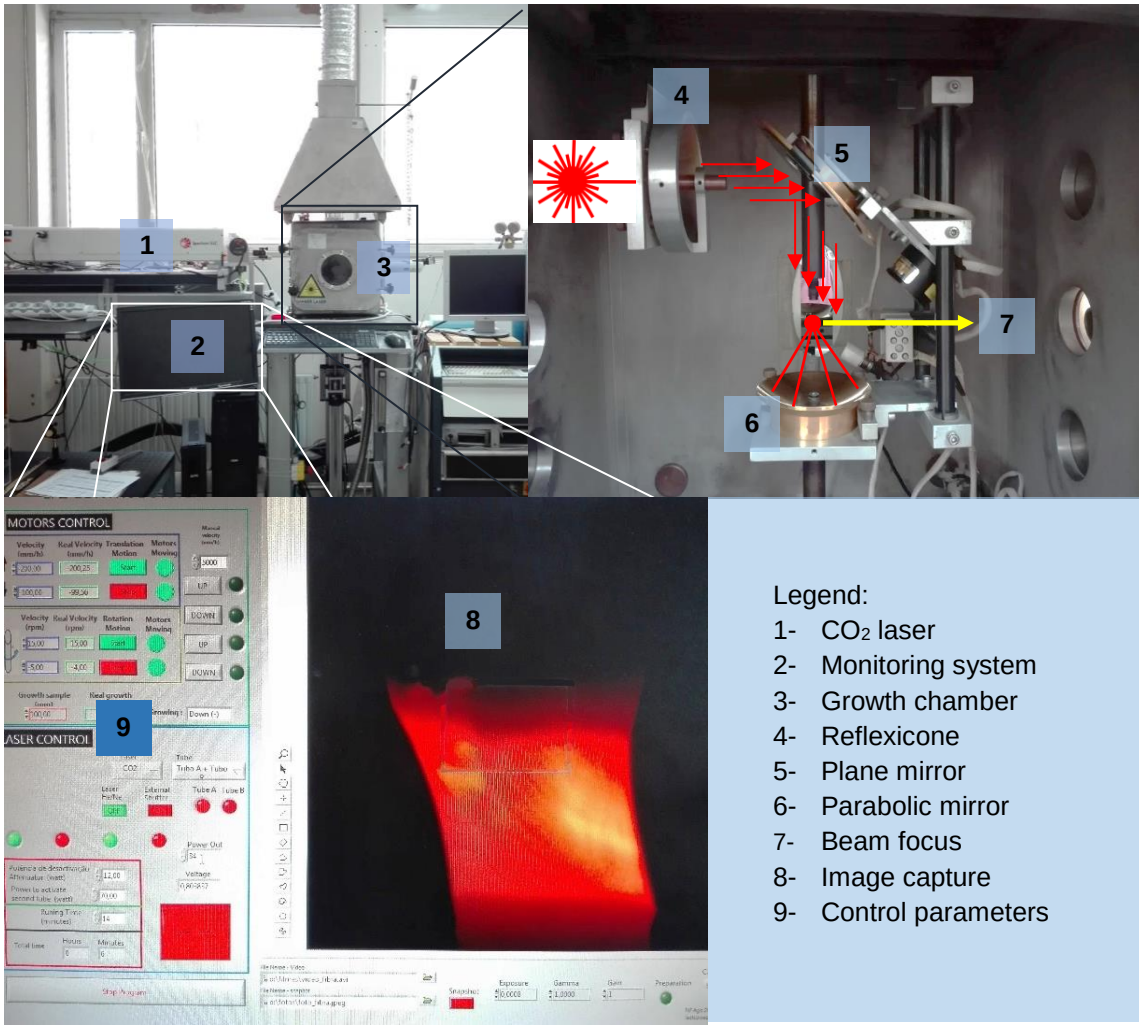

Figure 2.3 - LZF equipment setup with insets to the growing chamber and motoring system screen.

The growth chamber (3) allows the use of different gas atmospheres and pressures. To melt uniformly the feed/seed rods precursor, the laser beam is transformed into a circular crown-shape, using a reflexicone (4). Afterwards, it is reflected by planar mirror (5) towards parabolic mirror (6) that converges the beam to the top of the rod precursors, where all the beam laser power is located (7). The laser system must be sufficiently powerful to melt the material and maintain a stable condition of the molten zone. Also, constant melt material volume must be kept during the processing (height in the Fig. 2.4), since the crystal growth process is based on the mass conservation principle. This control is done via image capture (8) displayed in the monitoring system. The molten zone (red zone on the image capture) can be continuously measured and maintained as the growth process takes place.

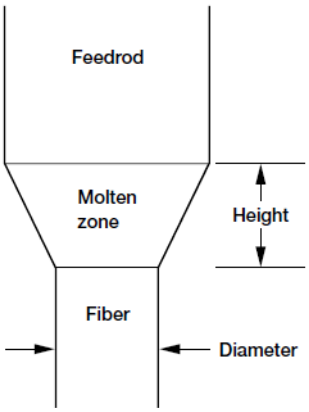

Figure 2.4 - Cross-section of LFZ working technique. Solid-liquid interface with schematic height of the molten zone and diameter of the grown fibre (Ritzert, 1996).

The growth process of the fibres followed the steps:

1. the extruded rod-like precursor fibre used as feed rod is positioned on the laser beam focus;
2. a seed rod is also positioned bellow the laser beam;
3. opposite rotation is applied to both motors;
4. laser is turned on and power increase creates a molten tip on the bottom of the feed rod;
5. the seed rod precursor is immersed into the melt;
6. laser power increase to form stable molten zone;
7. initiation of the pulling.

After growth initiation, the temperature of the pulled material decreases, leading to the change of the free energy and allowing the crystallization process. The rotation in opposite directions allow to homogenise the molten zone and was kept constant during this work.

Figure 2.5 shows the interior space of the growth chamber after processing of a fibre. The grown fibre (originated from the feed rod) “sits” on the top of the seed rod as it helped to immerse into the melt. Regardless every condition applied, the growth process followed the steps previously presented aiming to result in highly-dense fibres, as exemplified in next figure.

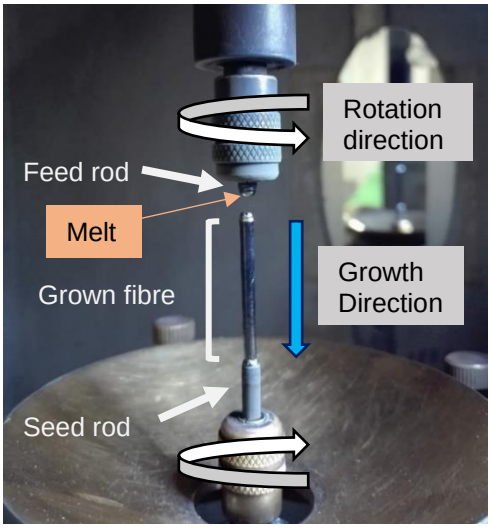

Figure 2.5 - LFZ growth chamber after processing with identification of the various regions of the processed fibre. Corresponding directions and rotations are also illustrated.

For this study, two principal growth parameters, the pulling rate and the chamber atmosphere were varied where different pulling rates were selected: 25, 100 and 200 mm h^{-1} and the growth atmosphere: firstly attempted in air, after in vacuum (12 mbar of pressure) and, finally, in argon. For pulling rate appliance, on the last step of the growth process, the pulling rate is selected, and the growth can be initiated while for the atmosphere, the chamber must be ready before the growth process can start.

2.3 PROCESSING CONDITIONS AND DENOMINATION OF THE SAMPLES

For further convenience, Table 2.1 presents the sample denominations of the fibres characterized, including description of chemical composition, LFZ processing conditions and thermal treatments. These denominations will be further used to refer and identify each sample based on the applied conditions. Samples are identified primarily with the selected level of praseodymium substitution. Thus, Pr3, Pr6 and Pr10 mean, respectively, 3, 6 and 10% referring to chemical composition: $Ca_{1-x}Pr_xMnO_3$ where x= 0,03; 0,06 and 0,10. This denomination is followed by the pulling rate applied, expressed as 200, 100 or 25 mm h^{-1} for each of the growth rates, growth atmosphere (air or argon (Ar)) and growth in vacuum. Finally, the annealing temperature (1573 K) are present on the denomination, if the corresponding treatment was performed.

Table 2.1 - Samples denomination, chemical composition and processing conditions.

Denomination	Chemical composition	Pulling rate, mm h^{-1}	Growth atmosphere	Post-treatment
Pr3_200mm	$Ca_{0.97}Pr_{0.03}MnO_{3-\delta}$	200	air	-
Pr6_200mm	$Ca_{0.94}Pr_{0.06}MnO_{3-\delta}$			
Pr10_200mm	$Ca_{0.9}Pr_{0.1}MnO_{3-\delta}$			
Pr3_100mm	$Ca_{0.97}Pr_{0.03}MnO_{3-\delta}$	100	air	-
Pr6_100mm	$Ca_{0.94}Pr_{0.06}MnO_{3-\delta}$			
Pr10_100mm	$Ca_{0.9}Pr_{0.1}MnO_{3-\delta}$			
Pr3_100mm_va	$Ca_{0.97}Pr_{0.03}MnO_{3-\delta}$	100	vacuum	-
Pr6_100mm_va	$Ca_{0.94}Pr_{0.06}MnO_{3-\delta}$			
Pr10_100mm_va	$Ca_{0.9}Pr_{0.1}MnO_{3-\delta}$			
Pr3_100mm_Ar	$Ca_{0.97}Pr_{0.03}MnO_{3-\delta}$	100	argon	-
Pr6_100mm_Ar	$Ca_{0.94}Pr_{0.06}MnO_{3-\delta}$			
Pr10_100mm_Ar	$Ca_{0.9}Pr_{0.1}MnO_{3-\delta}$			
Pr3_25mm	$Ca_{0.97}Pr_{0.03}MnO_{3-\delta}$	25	air	-
Pr6_25mm	$Ca_{0.94}Pr_{0.06}MnO_{3-\delta}$			
Pr10_25mm	$Ca_{0.9}Pr_{0.1}MnO_{3-\delta}$			
Pr3_100mm_1573K	$Ca_{0.97}Pr_{0.03}MnO_{3-\delta}$	100	air	1573 K (10h) in air
Pr6_100mm_1573K	$Ca_{0.94}Pr_{0.06}MnO_{3-\delta}$			
Pr10_100mm_1573K	$Ca_{0.9}Pr_{0.1}MnO_{3-\delta}$			
Pr3_25mm_1573K	$Ca_{0.97}Pr_{0.03}MnO_{3-\delta}$	25	air	1573 K (10h) in air
Pr6_25mm_1573K	$Ca_{0.94}Pr_{0.06}MnO_{3-\delta}$			
Pr10_25mm_1573K	$Ca_{0.9}Pr_{0.1}MnO_{3-\delta}$			

2.4 CHARACTERIZATION TECHNIQUES

In terms of techniques, relevant studies on the structure and microstructure were conducted, including phase identification and analysis and morphology. For thermoelectric properties, characterization included measurements of the electrical conductivity and Seebeck coefficient, each technique is described next.

X-Ray diffraction

The phase composition of prepared samples was analysed by X-ray powder diffraction. Spectra was recorded using PANalytical - X'pert-PRO diffractometer (CuK$_\alpha$ radiation) at room temperature with a target source of X-ray of copper, in which the wavelength of the radiation K$_{\alpha1}$ is 1,54060 and of K$_{\alpha2}$ is 1,54443 Å. The scan range was from 2θ = 10 - 80˚, with a step size of 0.0263. XRD analysis is based on constructive interference of monochromatic X-rays and a crystalline sample. The X-rays are generated by a cathode ray tube, filtered to produce monochromatic radiation, collimated to concentrate, and directed toward the sample. The interaction of the incident rays with the sample produces constructive interference (and a diffracted ray) when conditions satisfying Bragg's Law *($n\lambda=2d\ sin\ \theta$)* (see Fig. 2.6A). This law relates the wavelength of electromagnetic radiation to the diffraction angle and the lattice spacing in a crystalline sample. Diffracted rays are then directed to the detector as Figure 2.6B shows. The characteristic X-ray diffraction pattern generated during a typical XRD analysis provides a unique "fingerprint" of the sample structure.

When properly interpreted, by comparison with standard reference patterns and measurements, this fingerprint allows identification of the crystalline form. By comparison with diffraction patterns recorded in specific database JCPDS files, the obtained diffraction patterns can be interpreted, and the crystallographic phases can be identified.

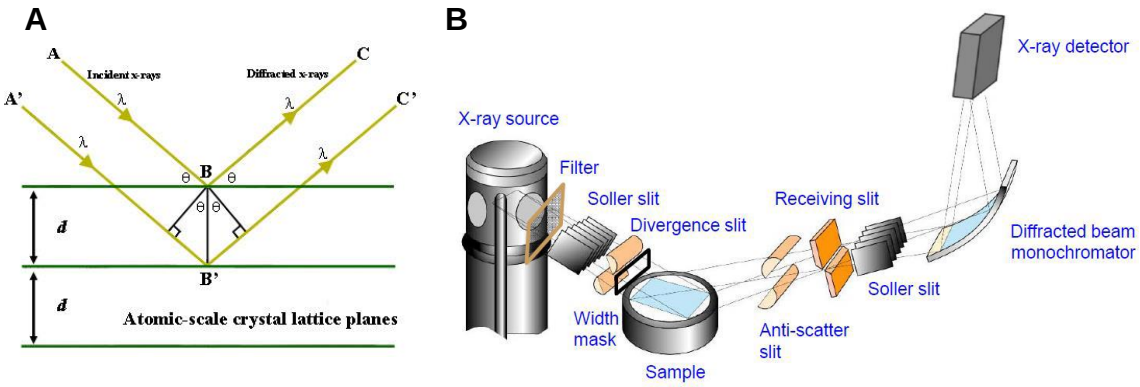

Figure 2.6 - Bragg's Law reflection: the diffracted X-rays exhibit constructive interference when the distance between paths ABC and A'B'C' differs by an integer number of wavelengths (*λ*), A. X-ray diffraction analysis scheme, B.

SEM/EDS

Morphology analysis was performed by Scanning Electron Microscopy (SEM) using a *Hitachi SU-70* equipment (Fig. 2.7). In this technique, the surface of a specimen to be examined is scanned with an electron beam, and reflected (or back-scattered) beam of electrons is collected and then displayed, at the same scanning rate, through an image on a screen that represent the surface features of the specimen. The surface may or may not have been polished and etched, but it must be electrically conductive. For nonconductive materials, a very thin metallic or carbon layer must be applied.

Accessory equipment allowed qualitative and semi quantitative analysis of the chemical composition in localized areas, namely, by Energy Dispersive X-ray Spectroscopy (SEM-EDS). In this work, SEM/EDS analysis was used for morphological and chemical analysis of samples gown by LFZ method. A fibre to analyse was fractured and impregnated in a mixture composed by a hardener and a resin. After impregnation, samples were polished with abrasive papers and diamond pastes. Top and cross-section sample parts were analysed.

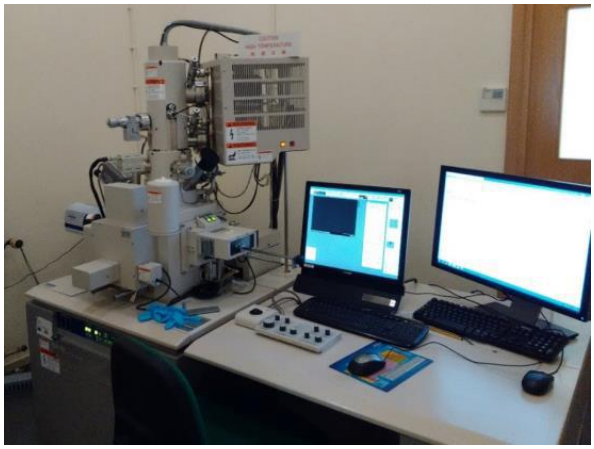

Figure 2.7 – SEM Hitachi SU-70.

Density

Apparent density ρ, was analysed for the grown fibres. Measurements were done based on geometrical dimensions of the sample and its weight as:

$$\rho = \frac{m}{v} = \frac{m}{l \times A} \qquad \text{Eq. 11}$$

where *m* is the mass, *v* is the fibre volume, also described as the length of the fibre *(l)* and the cross-section area *(A).* An average of 5 measurements performed for the fibres of a given nominal chemical composition processed under similar conditions was considered as a final density.

Electrical Conductivity and Seebeck coefficient

Two different fibres with the same chemical composition and processed under similar conditions (or, preferably, prepared by fracturing of one long fibre) were used for these studies.

The horizontal sample under minimal thermal gradient was employed for electrical conductivity measurement. A four-probe DC method was used for electrical conductivity measurements, as it is commonly accepted for thermoelectric materials normally possessing the electrical conductivity fairly above 1 S cm^{-1}. Eq. 12 describes how the electrical conductivity (σ) was calculated in the present work, namely, by applying a known electrical current (*I*) generating ae electrical potential difference (*U*) over a distance *L* in the fibre with cross-section area *A*.

$$\sigma = \frac{1}{\rho} = \frac{I}{U} . \frac{L}{A} \qquad \text{Eq. 12}$$

The current was applied through one set of Pt leads, while the voltage was measured using another set of Pt leads.

An example of the fibre sample with attached Pt leads is shown in Fig. 2.8A. The geometry of the lead-sample contacts is very important. Contacts were made by applying platinum-paint to the sample to ensure a good ohmic connection.

The fibre for Seebeck coefficient measurement was fixed in vertical position by a spring load force, in connection with two spiral Pt wires of S-type thermocouples (see Fig. 2.8B), embedded in alumina capillaries and also acting as thermal voltage probes. In order to provide precise temperature control, the distance between sample ends and thermocouple junctions did not exceed 0.5 mm. Temperature gradient along the length of the sample is set up by fine Pt wire heater, wound in grooves of the holder at the top side. Contribution of the offset voltage was checked by verifying the dependence of thermal voltage on the temperature gradient.

The measured value of thermopower (α_{sl}) includes the contribution of the sample (α_s) and measuring wires/leads (α_l) as:

$$\alpha_{sl} = \alpha_l - \alpha_s = \frac{V_h - V_c}{T_h - T_c} \qquad \text{Eq. 13}$$

where, V_h/T_h and V_c/T_c are potential and temperature at hot *(h)* and cold *(c)* sides, respectively. Thus, the thermally-induced potential difference, which corresponds strictly to the fibre sample, was extracted by correcting for known contribution of Pt leads.

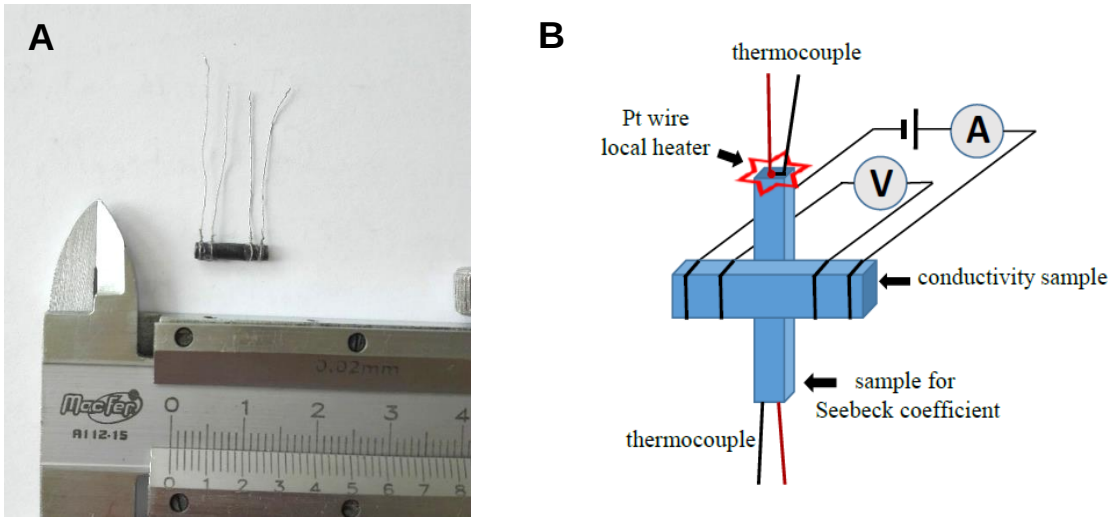

Figure 2.8 - Grown fibre used for electrical conductivity measurement showing the two pairs of leads, A; experimental setup for simultaneous measurements of electrical conductivity and Seebeck coefficient, B.

The measurements were done in flowing air on stepwise cooling from 1173 K to 523 K, followed by up to 0.5 hours thermal equilibration at each temperature, or *vs.* time in isothermal conditions. The isothermal measurements were performed to assess the long-term stability of the prepared materials under prospective operation conditions and even higher temperatures. The latter included registration of the electrical conductivity and Seebeck coefficient values over time at 1173 K for ~15 h.

CHAPTER 3

RESULTS & DISCUSSION

3 RESULTS & DISCUSSION

Producing of dense and mechanically-strong ceramics based on the proposed compositions is required both for correct studies of the thermoelectric properties and fabrication of the reliable thermoelectric modules. LFZ processing revealed certain challenges when selected conditions were applied. In the first place, an optimization to the growing conditions of the fibres was accessed as a crucial step for thermoelectric characterization.

3.1 CHALLENGES OF LFZ PROCESSING

Preliminary experiments on LFZ processing of $Ca_{1-x}Pr_xMnO_3$ samples revealed certain challenges, which had to be resolved before characterization by optimizing the growth conditions. As described in the previous chapter, pulling rates of 25, 100 and 200 mm h^{-1} were attempted together with different growth atmospheres, air, vacuum and argon. Figure 3.1A shows the result for a fibre grown at high rate of 200 mm h^{-1}. The visual inhomogeneity of the sample is the result of a non-stable molten zone maintenance during the growth. Higher thermal gradients are known to favour such morphology. Besides possible problems with the chemical and phase homogeneity, such fibre shape also preclude correct thermoelectric characterization, in particular, 4-probe DC measurements of electrical conductivity, which require a regular sample geometry. This shape also does not appear appropriate for a leg of thermoelectric module due to hardly predictable current distribution mechanical strength issues and difficulties in producing a closely packed assembly.

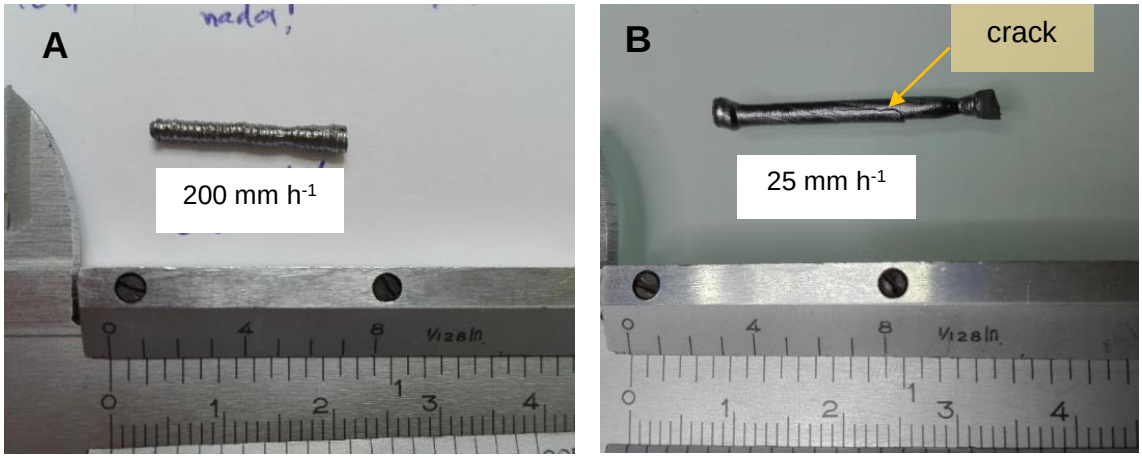

Figure 3.1 - Challenges of pulling rate conditions on LFZ: examples of inhomogeneities created at 200 mm h^{-1} (A) and fractures derived from 25 mm h^{-1} (B).

In contrast, opposing to the “fast” growing rates, when grown at 25 mm h^{-1}, the resulted fibres exhibit much more homogeneous shape, as shown in Fig. 3.1B. In most cases, slow pulling rates also produce crystals with superior crystallinity (Ritzert, 1996). However, these fibres were extremely fragile, resulting in cracks during preparation of the samples for measurements and even when carefully handled. Possible reasons for this may include presence of highly oriented crystallites loosely bound to each other along with the lattice stresses promoted by incorporation of praseodymium. The results of structural and microstructural analysis discussed in next chapter give some guidelines to explain the observed behaviour. Additional thermal treatment, as discussed below in chapter 3.4, was attempted for the samples grown at 25 and 100 mm h^{-1}, aiming, in particular, better mechanical strength of the material for further thermoelectric characterizations.

The growth atmosphere was also varied during the processing, for instance vacuum (~12 mbar) was applied on the growing chamber. However, non-stable molten zone was reproducibly observed under these conditions, impeding growth of appropriate fibres. Detailed characterization of the samples grown for all compositions is discussed below. Denominations of the samples studied are linked to the Table 2.1 in session 2.3.

3.2 STRUCTURAL AND MICROSTRUCTURAL PROPERTIES OF AS-GROWN FIBRES

In this section, the effect of LFZ processing conditions on phase composition, morphology, microstructural features of the grown samples will be discussed. Fig. 3.2 shows room-temperature XDR patterns for various compositions and different processing scenarios including pulling rates of 25 and 100 mm h^{-1} in air and Ar atmosphere.

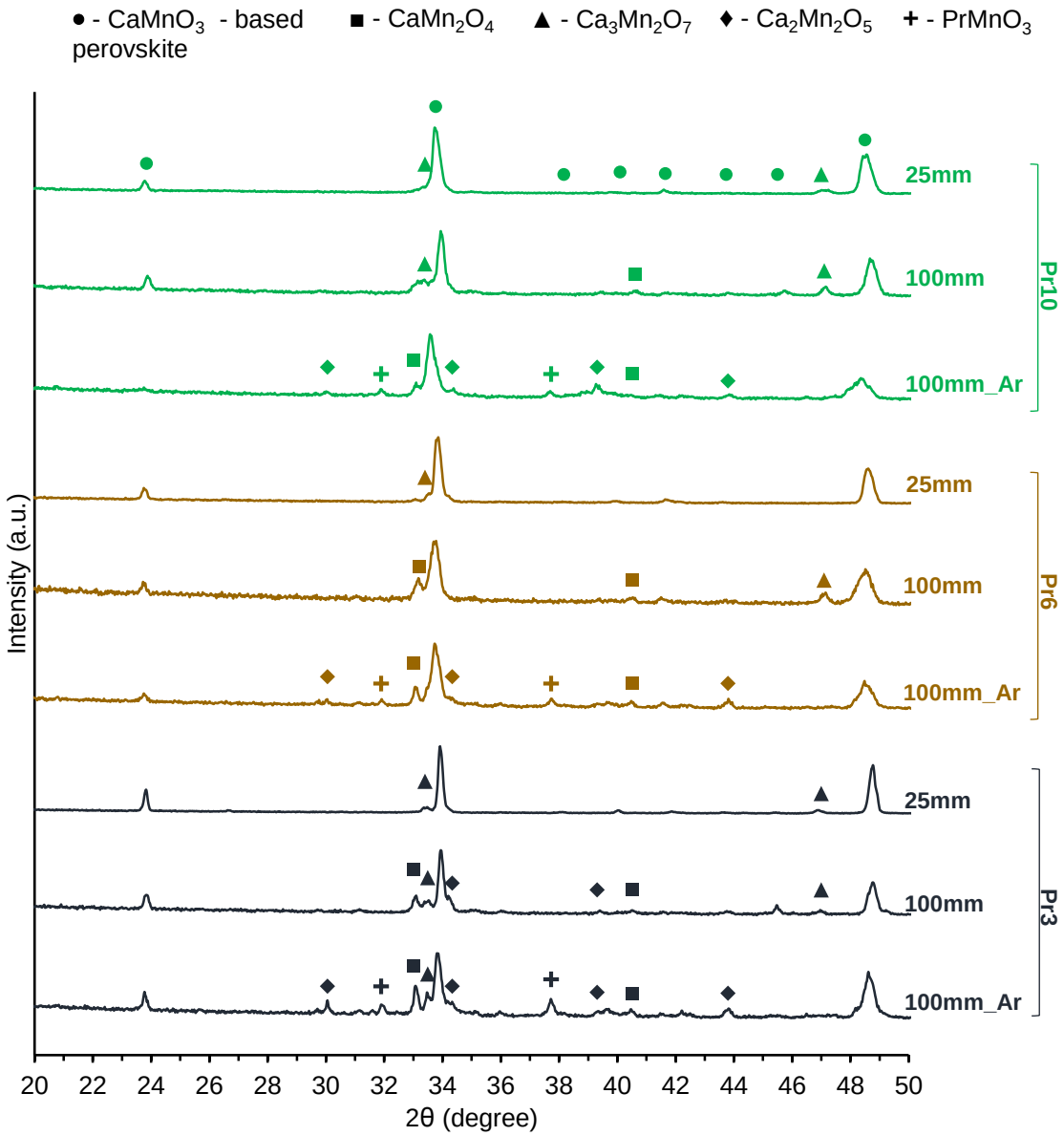

Figure 3.2 - Phase composition of the powdered samples of as-grown fibres, processed under various LFZ conditions.

The formation of perovskite-type calcium manganite phase, which actually represents the main interest in terms of the thermoelectric properties, was observed in all samples, indexed in accordance with standard JCPDS card No. 04-008-4530 for orthorhombic structure. Various secondary phases were also identified namely, including $CaMn_2O_4$ (04-009-8109), $Ca_3Mn_2O_7$ (04-015-9135), $Ca_2Mn_2O_5$ (00-036-0531), and praseodymium-rich $PrMnO_3$ phase (04-014-9589).

Presented data obviously indicate that strong non-equilibrium conditions imposed by LFZ processing in all cases result in non-single phase $(Pr,Ca)MnO_{3-\delta}$ ceramic fibres. The observed non-systematic shift of high intensity peaks (2θ = 23.8, 33.9 and 48.8°) to lower diffraction angles apparently indicates an increase in lattice parameter on praseodymium incorporation. The ionic radii of Pr^{3+} and Ca^{2+} cations are quite close (Shannon, 1976), while Pr^{4+} is notably smaller. It should be noticed that such dependence of the lattice parameter on praseodymium content is contradictory to the results presented in (Zhang, 2013), which suggests a lattice contraction on substitution with praseodymium. This can be attributed both to specificity of LFZ processing which favours frozen-in lower oxidation states of redox active cations, as compared to the traditional ceramic route used in (Zhang, 2013), and even more to the complex phase composition where the actual substitution level is unknown. In several cases, the width of the diffraction peaks tends to become slightly broader, which can indicate grain size decrease (Zhang, 2013).

In general, the XDR results for as-grown fibres suggest that slower pulling rates and correspondingly, higher temperature gradients (Abe, 2000), are favourable for the formation of perovskite-type phase with desired thermoelectric properties. The samples grown at lowest rate of 25 mm h^{-1} are also expected to have superior crystallinity (Ritzert, 1996)(Costa FM, Carrasco FG, Silva RF, 2005). Argon atmosphere favours formation of secondary phases identified as various calcium manganese oxides and even praseodymium manganese oxide. Most likely, mildly-reducing conditions like Ar promote excessive reduction of manganese cations, especially at extreme high temperatures promoted by the LFZ process. This may facilitate the phase separation and, in particular, the formation of $PrMnO_3$ involving lower manganese oxidation state as compared to $CaMnO_3$. Such behaviour can be seen in Pr3, Pr6 and Pr10 100mm_Ar patterns where $Ca_2Mn_2O_5$ and $PrMnO_3$ phases are identified. In several cases calcium-rich $Ca_3Mn_2O_7$ and manganese-rich $CaMn_2O_4$ secondary phases appear providing a self-compensation effect for calcium distribution in the formed phases. Also, the formation of secondary phases and, therefore, appearance of various interfaces may be favourable for the thermal conductivity, this leads to significant deviations in the composition of calcium manganite-based perovskite phase, which is not good for electrical properties, as discussed further.

Table 3.2. presents the density values measured for as-grown fibres at 100mm h^{-1} and 100mm h^{-1} in Ar atmosphere. Due to complex phase composition it was difficult to estimate the theoretical density of the fibres. However, the listed values are comparable to the theoretical density $CaMnO_3$ calculated from XDR data, which corresponds to 4.59 g cm^{-1} (Villars, n.d.)(Celorrio, 2016)(Han, 2013).

Table 3.1 - Density, ρ (g cm^{-3}), measured in as-grown fibres.

Pulling rate / Pr content	100mm	100mm_Ar
Pr10	4.50	4.79
Pr6	4.57	4.56
Pr3	4.37	4.44

This indicates that the grown fibres are very dense. The work (Zhang, 2013) suggests that the relative density should increase with praseodymium content. The samples grown in Ar atmosphere exhibit higher density, apparently affected by more complex phase composition.

The results of detailed microstructural characterization, performed for all samples processed by laser, mainly confirm the general guidelines obtained from XRD analysis. The micrographs presented in Fig. 3.3 suggest an appearance of unique microstructural features, promoted by specificity of LFZ conditions, namely, the formation of core-shell structures.

The presence or absence of such core-shells most likely depends on many factors, including the growth conditions, atmosphere and chemical composition of the samples. However, no clear guidelines describing the effects of the above parameters were not yet obtained. The formation of similar structures was previously observed for magnetite/hematite system processed by LFZ (Ferreira, 2018b)(Ferreira, 2013). The work (Ferreira, 2018b) highlighted the importance of kinetics of melt crystallization, nuclei formation and heat transfer for the thickness and morphology of the composite Fe_3O_4/Fe_2O_3 core-shells. The obtained $(Ca,Pr)MnO_{3-\delta}$ -based core-shells have different thicknesses varying from several hundred µm (Fig. 3.3B) to ~50 µm (Fig. 3.3C) and ~10-20 µm (Fig. 3.3D), while more homogeneous fibre structure was formed in the case of Pr3_100mm_Ar (Fig. 3.3A). However, it seems that higher thermal gradients during the slow LFZ processing favor the formation of thinner core-shell structures (Fig. 3.3D).

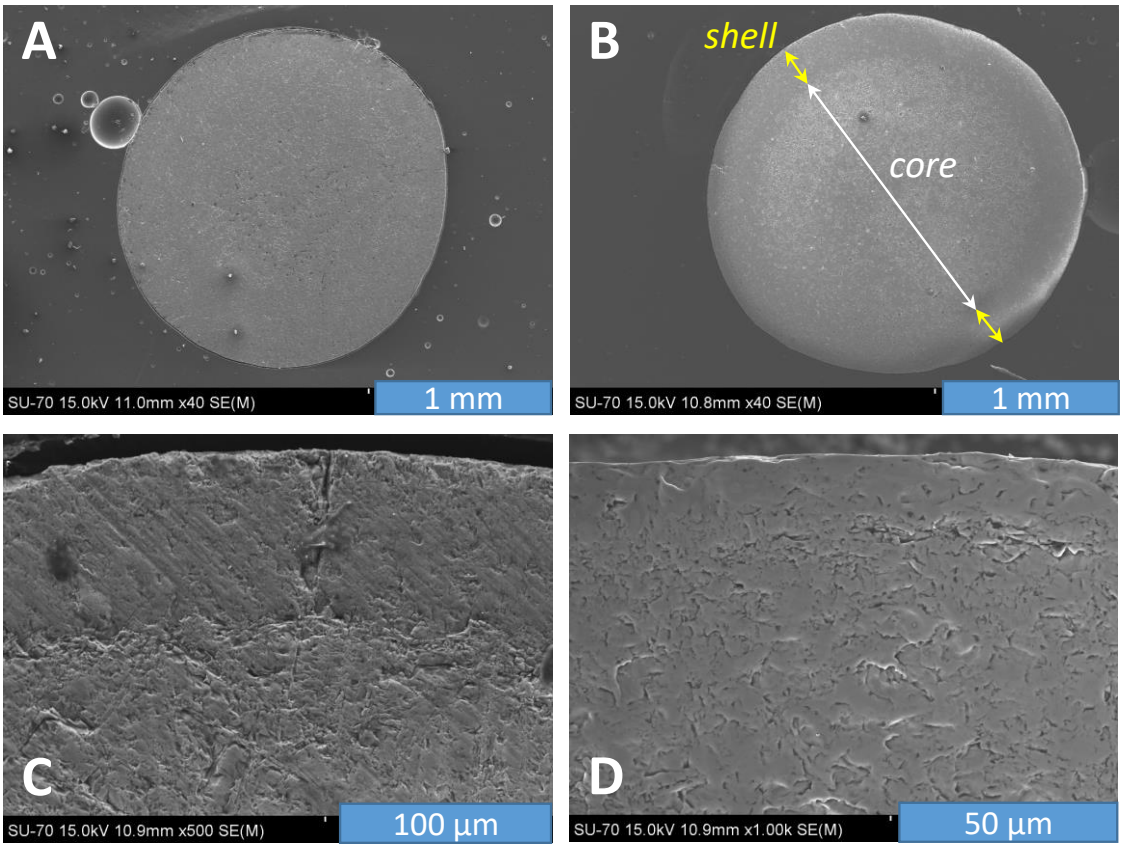

Figure 3.3 - Low-resolution SEM micrographs of transverse section of the as-grown fibres: Pr3_100mm_Ar (A), Pr10_100mm_Ar (B), Pr6_100mm (C) and Pr10_25mm (D).

According to the results of combined SEM/EDS analysis (Fig. 3.4), the core and shell have a very similar chemical composition at macro-scale, although the differences in oxygen nonstoichiometry between oxide phases in the core and outer layer should not be excluded (Ferreira, 2018b)(Ferreira, 2013). The shell layer also appears to be denser as compared to the core, except some residual porosity at the surface (Fig. 3.4). Considering thermoelectric

applications at high temperatures, especially in atmospheres containing CO_2 excess, the latter might be favorable for protection against interaction of Ca cations with the moisture and carbonate formation, thus avoiding degradation of the thermoelectric performance. Moreover, such microstructural inhomogeneities in radial direction may allow suppressing the lateral heat losses and are expected to affect the overall heat transport in tunable manner, provided by suitable altering of the laser processing conditions and growth atmosphere (Ferreira, 2018a).

Fig. 3.5 shows some typical SEM micrographs of the fibres grown in Ar and air atmospheres under different pulling rates. Laser processing in Ar results in pronounced growth of dendrites (Fig. 3.5A, B), quite typical for the LFZ process (Costa, 2001). However, they may be also considered as a fingerprint of phase inhomogeneities present in the sample, in accordance with the results of the XRD studies (Fig. 3.2), which showed that processing in Ar promotes the phase separation. As compared to the air-grown fibres (Fig. 3.5C, D), the formation of dendrites is also promoted by the oxygen-lean atmosphere and increasing the praseodymium content. The borderline of the stability *(*$p(O_2)$) vs. *T* diagram of $CaMnO_3$ at 1323 K corresponds to $p(O_2)$ = 0.026 atm and tends to increase with the temperature (Bakken, 2005). Therefore, simultaneous formation of calcium-rich $Ca_3Mn_2O_7$ and manganese-rich $CaMn_2O_4$ phases under LFZ conditions is facilitated in Ar atmosphere.

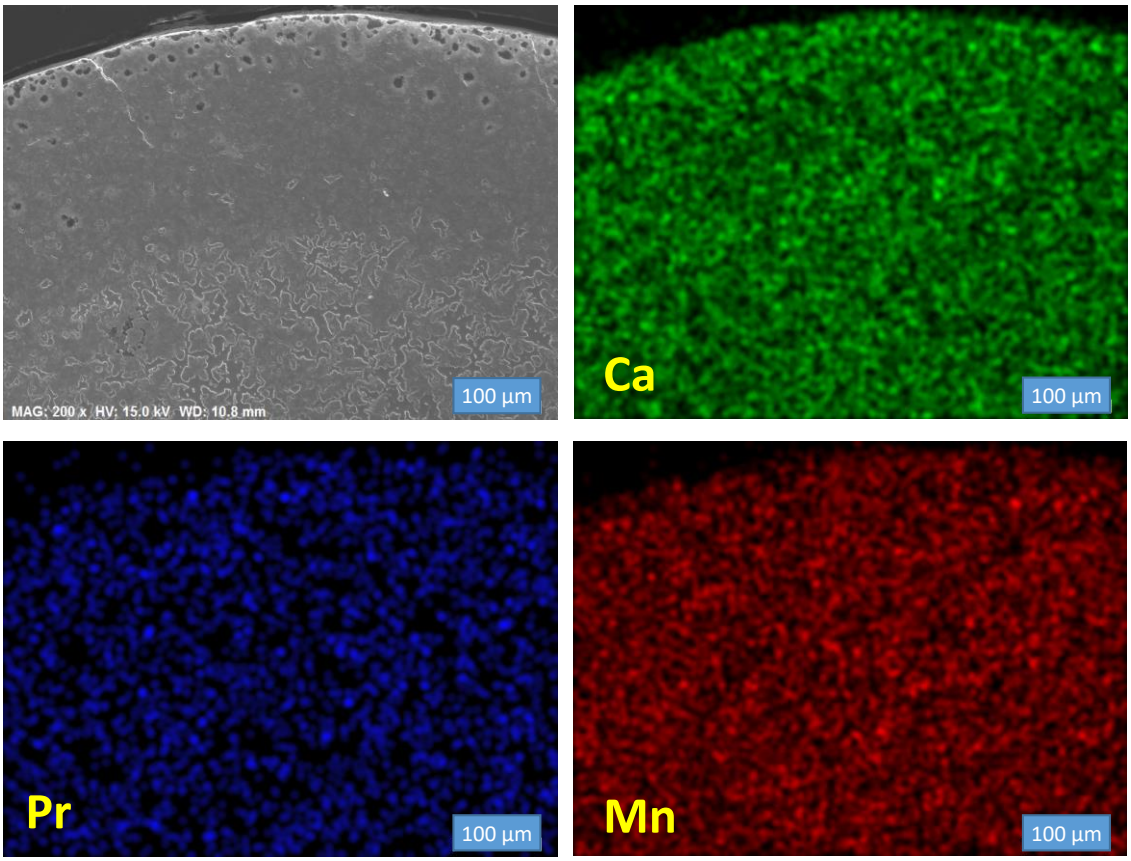

Figure 3.4 - Low-resolution SEM image and chemical mapping results for transverse section of the as-grown Pr10_100mm_Ar sample.

The air-grown samples (Fig. 3.5C, D) show more homogeneous microstructure. As it might be expected for such processing, the formation of elongated crystals (marked with arrows) along the growth direction is promoted by slower pulling rate (Fig. 3.5D). These crystals also appear to be denser compared to other areas of the fibre.

The EDS mapping (Fig. 3.6) results obtained for longitudinal section of as-grown Pr10_100m_Ar fibres confirm the above observations regarding the phase composition and are in agreement with the XRD results (Fig. 3.2).

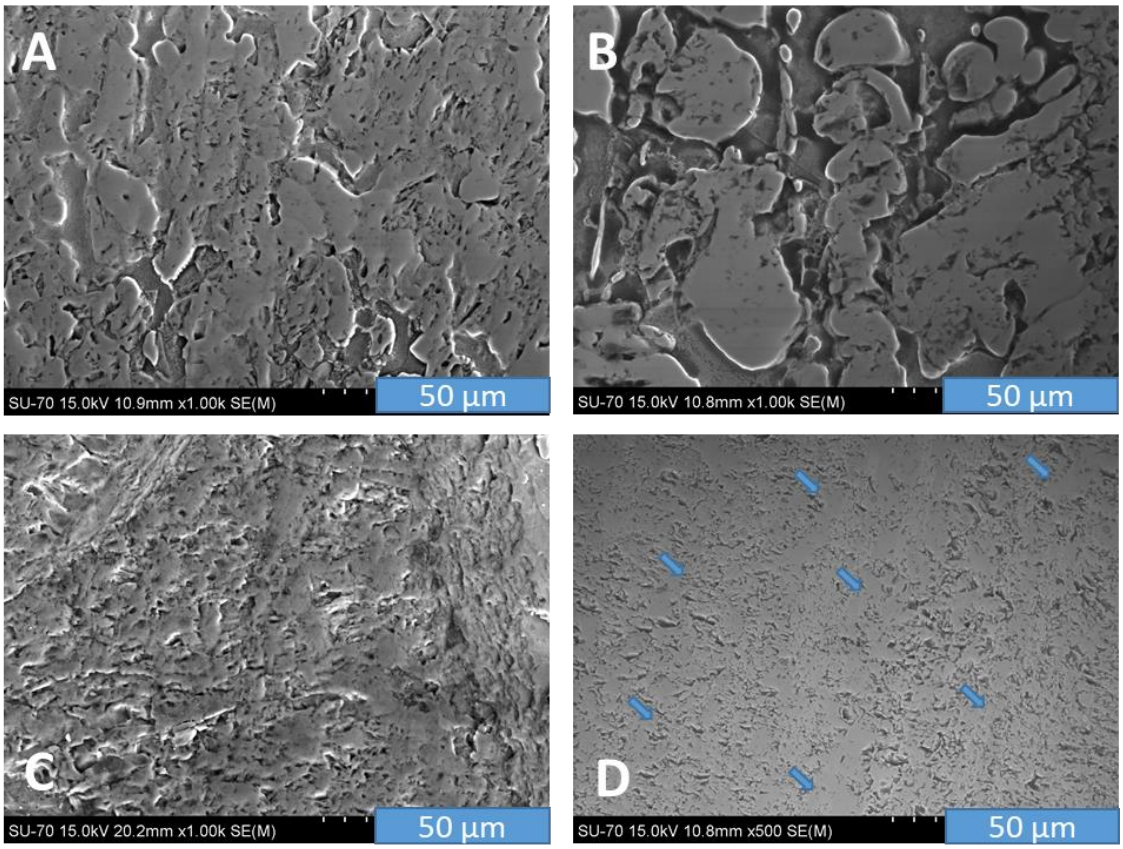

Figure 3.5 - Low-resolution SEM micrographs of longitudinal section of the as-grown fibres: Pr3_100mm_Ar (A), Pr10_100mm_Ar (B), Pr10_100mm (C) and Pr10_25mm (D).

The brighter dendrites enriched with praseodymium and possessing more or less uniform distribution of calcium and manganese cations most likely correspond to the $PrMnO_3$ phase identified in XRD patterns (Pr tends to migrate to Mn enriched sites when valance is Mn^{3+} opposing to Mn^{4+} as well as the $Ca_2Mn_2O_5$ phase instead of perovskite-type $(Ca,Pr)MnO_{3-\delta}$ structure, desirable for imparting reasonable thermoelectric properties). Several Mn-rich and Ca-rich areas apparently indicate the presence of $Ca_3Mn_2O_7$ and $CaMn_2O_4$ phases, as suggested by the XRD results. Presence of such texturing and apparent percolation of the brighter crystals may be favourable for enhanced mobility of the charge carriers. Still, the amount of phase impurities is too significant to expect a good thermoelectric performance.

Fig. 3.7 presents an enlarged area of Pr10_25mm fibre containing elongated darker crystals marked in Fig. 3.5D. The results of EDS mapping suggest that the contrast of chemical composition for this fibre, grown in the air, is somewhat similar to that for Ar-grown sample (Fig. 3.6). Although the presence of Pr- and Ca- and, probably, Mn-rich zones is again observed, the chemical composition of air-grown sample appears to be more homogeneous, in accordance with the XRD results (Fig. 3.2). Moderate texturing, again, is expected to have a positive effect on the thermoelectric performance. These observations were indirectly confirmed by preliminary measurements of the electrical properties, mainly, electrical conductivity, and are discussed in the sections 3.4-3.6. In particular, the studies revealed a noticeable increase of electrical conductivity for as-grown fibres with time at temperatures above ~900 K. This indicates that the phase composition of as-grown fibres tends to equilibrate on heating, actually leading to a better thermoelectric performance. Therefore, the as-prepared fibres were subjected to thermal treatment at higher temperatures; corresponding results of structural and microstructural characterization are described in section 3.3.

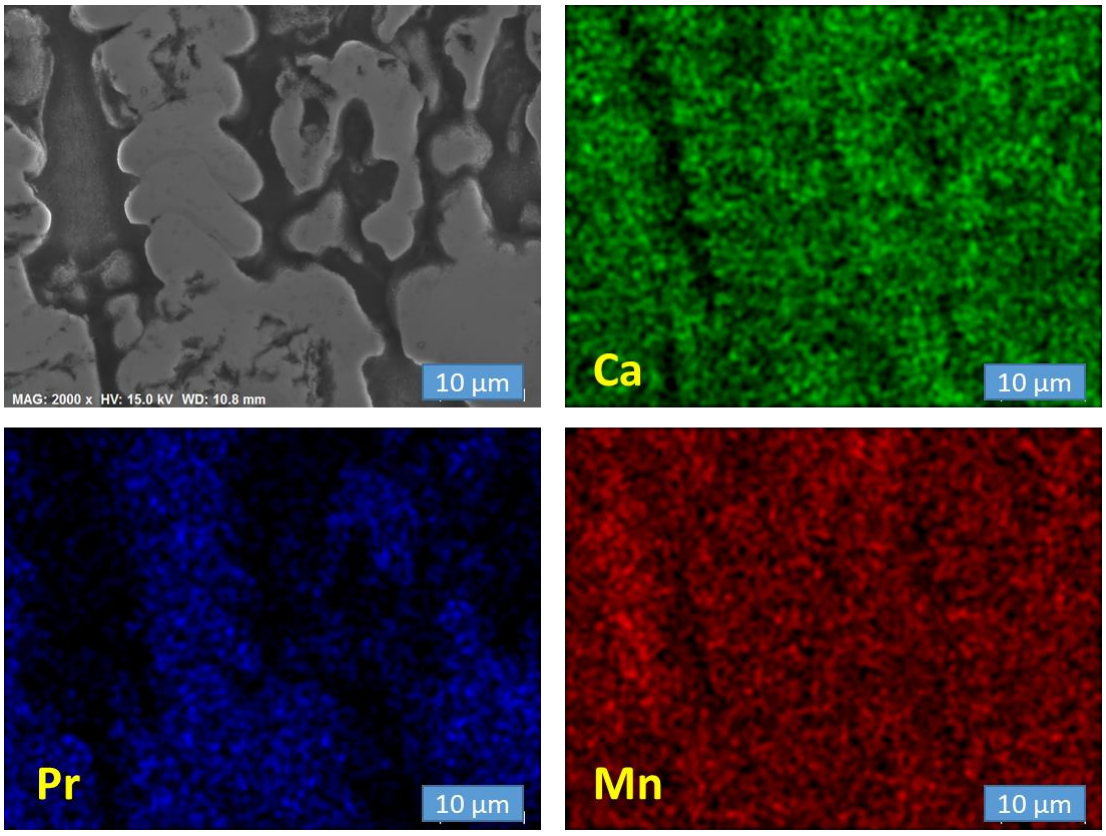

Figure 3.6 - Low-resolution SEM image and chemical mapping results for longitudinal section of as-grown Pr10_100m_Ar fibres.

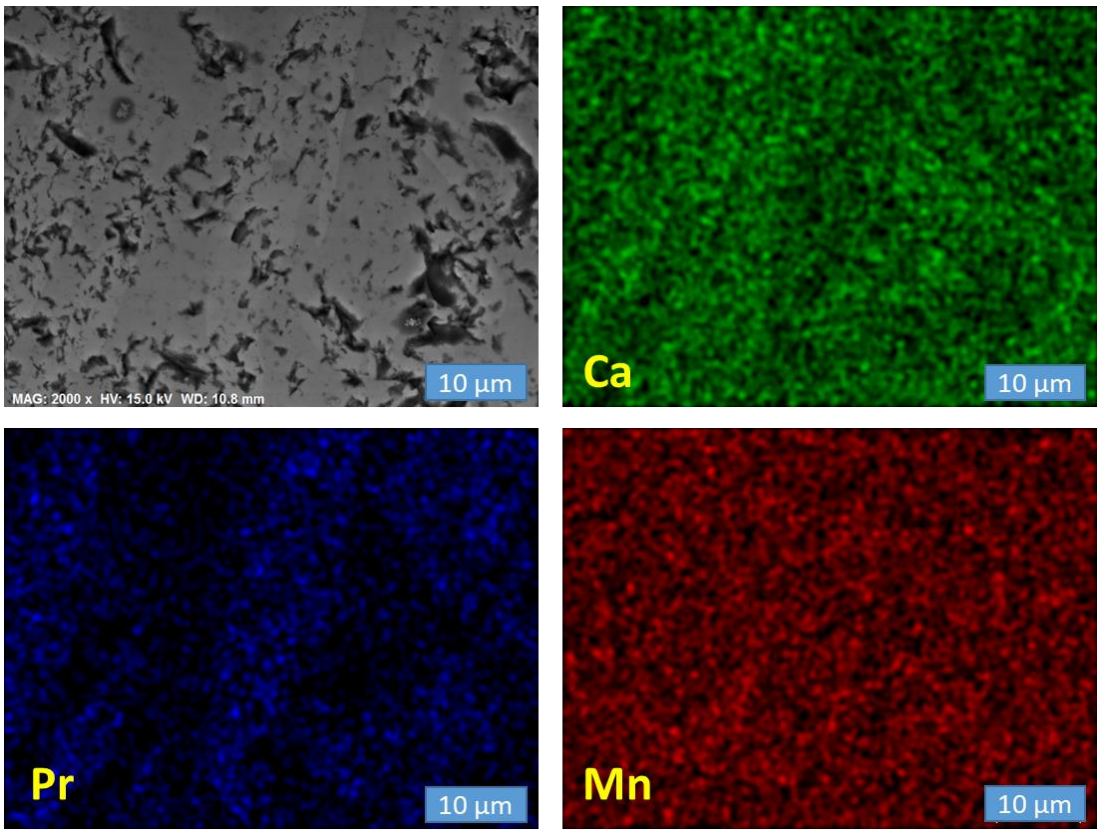

Figure 3.7 - Low-resolution SEM image and chemical mapping results for longitudinal section of as-grown Pr10_25mm fibres.

3.3 EFFECTS OF THE THERMAL TREATMENT ON COMPOSITION AND MICROSTRUCTURE

The optimal conditions for thermal treatments aiming at equilibration of the phase composition and increase of the mechanical strength increase of as-grown fibres were selected based on preliminary experiments. Fig. 3.8 shows the XDR pattern evolution with the annealing temperature from 1373 to 1573 K for a fibre with 3% of Pr substitution grown at 100 mm h^{-1}.

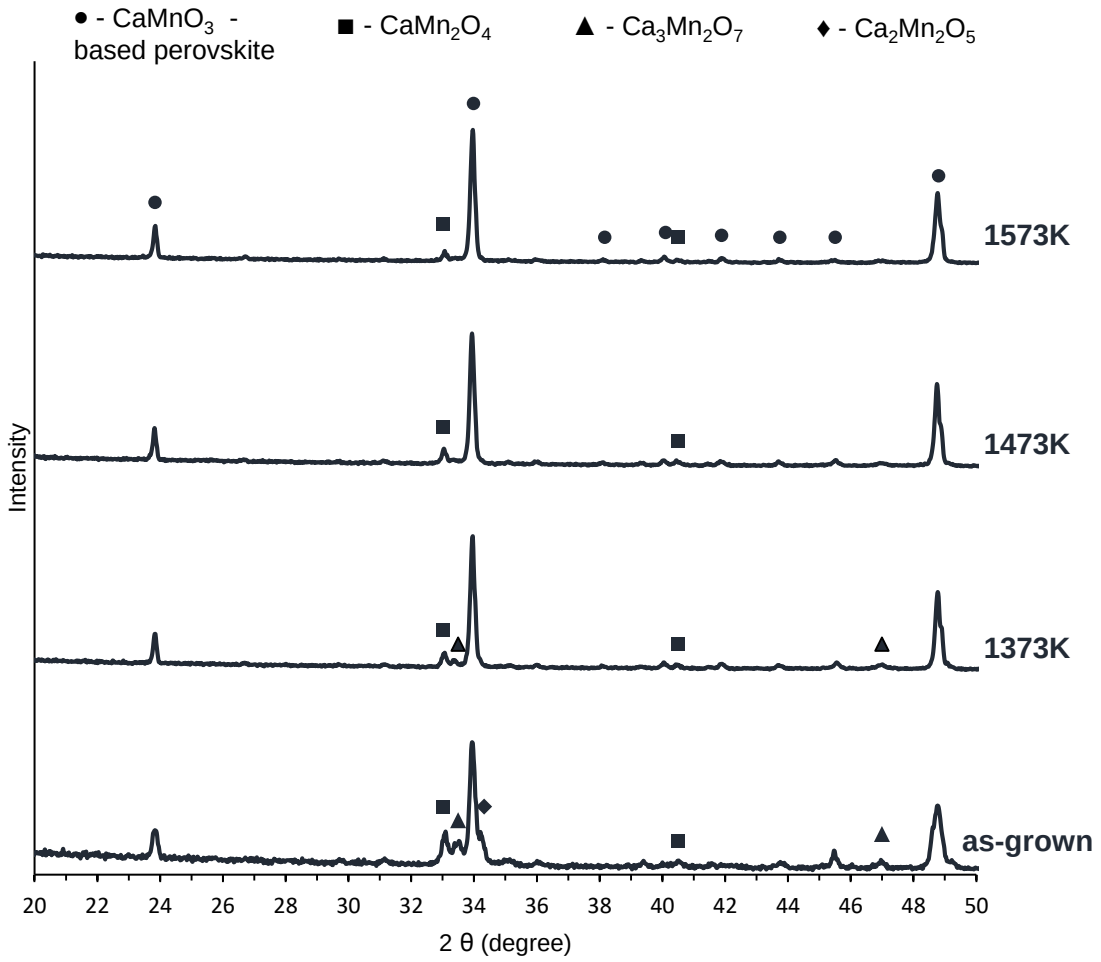

Figure 3.8 - Evolution of phase composition of as-grown Pr3_100mm composition fibres on thermal treatment at 1373, 1473 and 1573 K.

Significant decrease in impurity phases ($CaMn_2O_7$, $CaMn_2O_4$ and $Ca_2Mn_2O_5$) content was observed for the fibres annealed at 1573 K for 10 h. Given conditions allowed the homogenization of the phase composition by gradual evolution to a perovskite-type structure with best thermoelectric properties. Further increase in the annealing temperature leads to partial melting of the sample. Therefore, these conditions (air, 1573 K for 10h) were finally selected as thermal treatment conditions to demonstrate the effects of re-equilibration of the phase composition of the fibres on structural, microstructural and electrical properties. Since the results obtained for as-grown fibres have demonstrated that LFZ processing in Ar atmosphere results in too significant phase inhomogeneities, only fibres grown in air (25mm h^{-1} and 100 mm h^{-1}) were used for these studies.

Fig. 3.9 shows the phase composition of fibres, grown in air at different pulling rates, followed by thermal treatment. As compared to as-grown fibres (Fig. 3.2), the phase composition was significantly improved. The remaining minor peaks can be attributed to the same $CaMn_2O_4$ phase, also identified in as-grown samples.

These results confirm the re-equilibrium of phase composition, generated by strongly non-equilibrium conditions applied by LFZ technique. The 2θ shift of the peaks is decreased as compared to as-grown samples (Fig. 3.2), suggesting that the thermal treatment conditions provide rearrangement on the lattice structure and therefore, more homogeneous incorporation of Pr. However, the differences in the patterns for the same Pr concentration suggests that the LFZ pulling rate growth conditions applied still influences the structure even after a thermal treatment at 1573 K for 10h. As seen in Fig. 3.9, the presence of a secondary phase is noticeable.

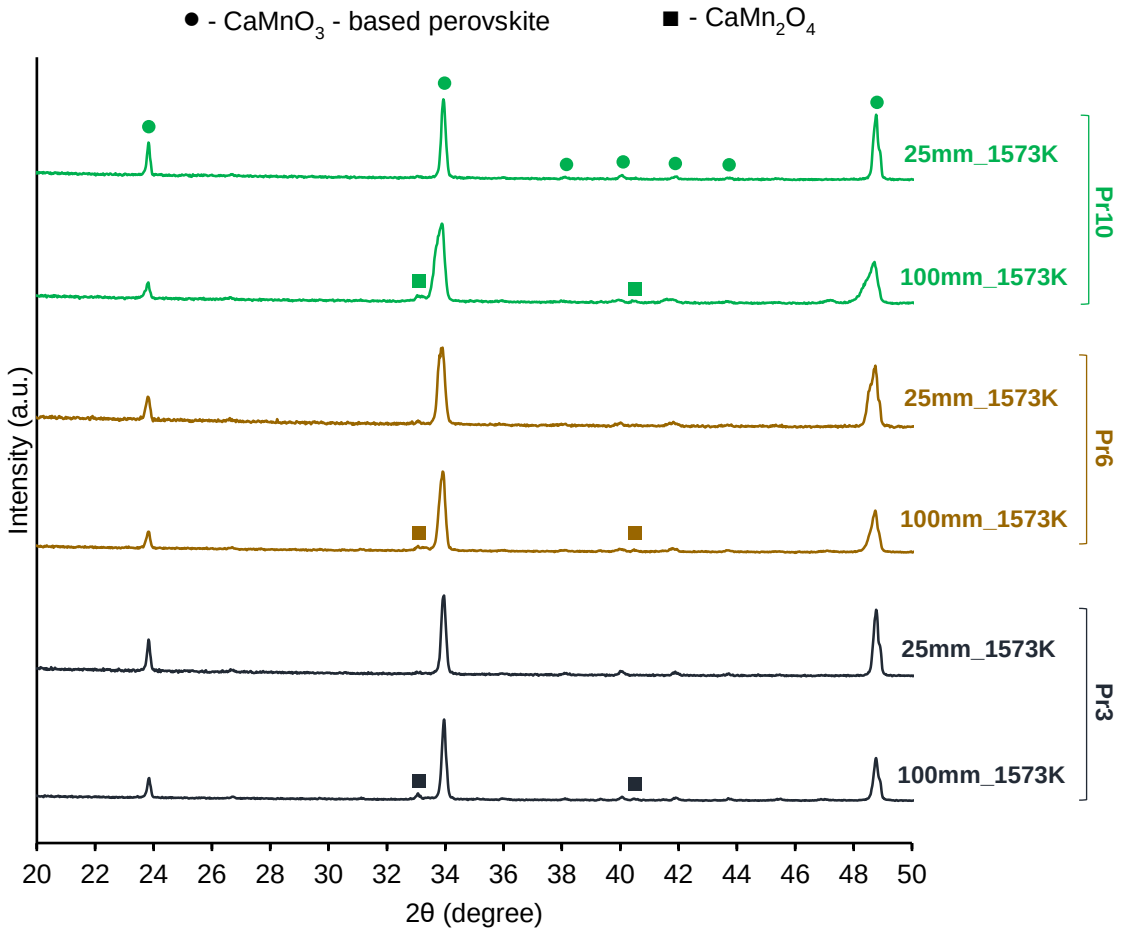

Figure 3.9 - XRD diffraction patterns of the fibres grown in air and annealed in air at 1573 K for 10 h.

Table 3.3 presents the densities of thermally treated fibres. In most cases, the density decreases after thermal treatment. This decrease occurs due to the progressive phase changes observed in the XRD patterns when comparing the as-grown and thermally treated fibres (Fig. 3.2 and 3.9). For slower pulling rates, highest density is observed for all thermally-treated samples, in agreement with known observation that lower pulling rate result in more homogeneous and dense materials. Moreover, pulling rates still maintain the ability to texturize the material. The observed tendency is also in agreement with the difference in densities between as-grown fibres with various content of phase impurities. In particular, the fibres (Table 2.2) grown in Ar and possessing the highest amount of impurities also showed higher density compared to the as-grown samples containing less impurities.

In opposite to as-grown fibres, the formation of core-shell structures were rarely observed in thermally treated samples and included the formation essentially thin shells, again confirming that the core-shells are promoted rather by oxygen-lean LFZ processing and slow pulling rate (Fig. 3.10).

Table 3.2 - Density, ρ (g cm^{-3}), measured in thermally treated fibres.

Pulling rate / Pr content	100mm_1573K	25mm_1573K
Pr10	4.49	4.84
Pr6	4.49	4.70
Pr3	4.01	4.62

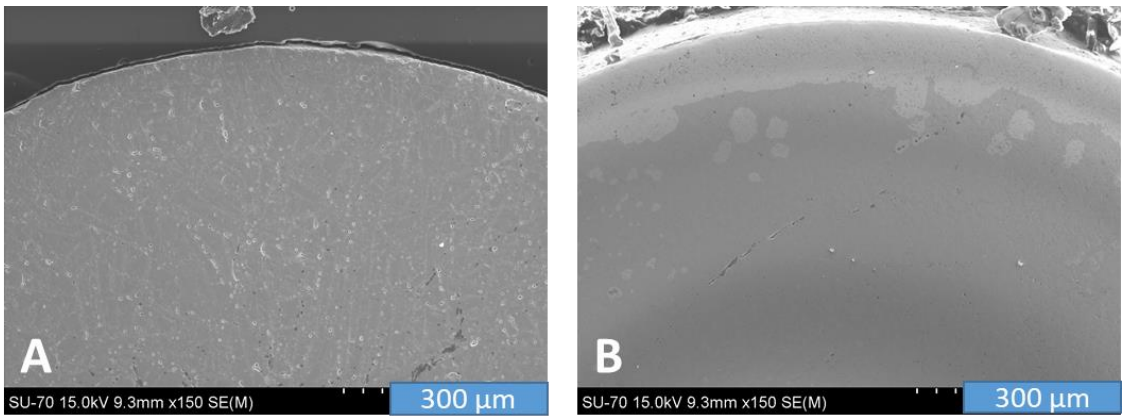

Figure 3.10 - Low-resolution SEM micrographs of transverse section of the thermally treated fibres: Pr6_100mm_1573K (A) and Pr10_25mm_1573K (B).

The SEM studies (Fig. 3.11) and EDS mapping results (Fig. 3.12) of longitudinal section of the thermally treated fibres show more uniform phase composition compared to as-grown fibres, indicating that the phase composition is re-equilibrated and desired perovskite-type phase is mostly formed. For fibres grown at 100 mm h^{-1} annealed at 1573 K (Fig. 3.11C) shows much homogeneous morphology compared with the same composition as-grown fibre (Fig. 3.5C).

Although the observed microstructural evolution is in a good agreement with the XRD results (Fig. 3.9), it seems that the performed thermal treatment is not sufficient for full homogenization of the chemical composition and morphology. Several local inhomogeneities and crystals, enriched in praseodymium and similar to those formed in as-grown fibres, are still present. Additional studies (probably, TEM) are required to correlate these inhomogeneities with the phases observed by XRD. Anyway, the results clearly confirm that the phase composition of LFZ-grown fibres can be significantly improved by post-processing, including a thermal treatment at 1573 K for 10 h. Relevant effects of such post-processing on the thermoelectric performance are discussed below.

3.4 ELECTRONIC TRANSPORT

This section presents the characterization of the electrical part of the thermoelectric performance aiming the demonstration of LFZ processing effects on the relevant properties. Total electrical conductivity and Seebeck parameters were measured in air on cooling for a range of temperatures from 500 to 1200 K. Power factor data is also plotted as a function of temperature for all measured samples. Direct impact of the LFZ processing on the thermoelectric performance is accessed and discussed based on previous structural and microstructural analysis.

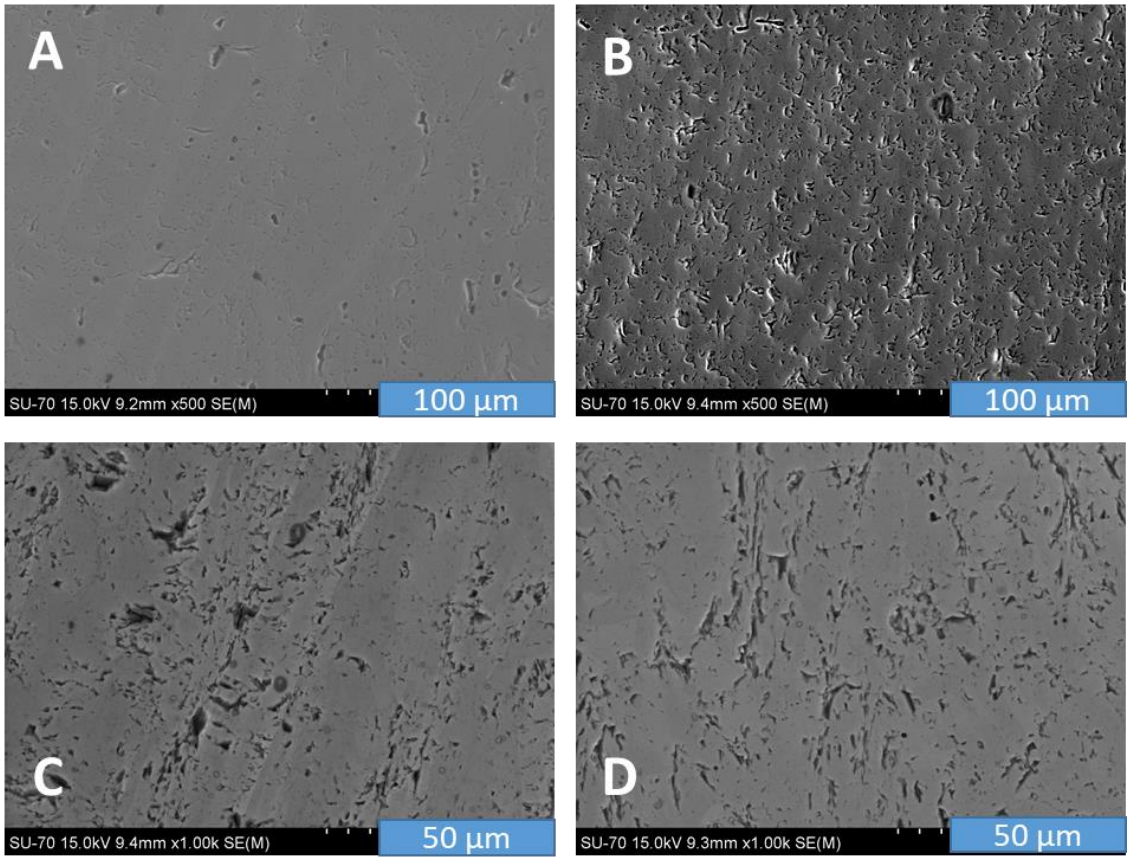

Figure 3.11 - Microstructure of the longitudinal section of the thermally treated fibres: Pr6_100mm_1573K (A), Pr6_25mm_1573K (B), Pr10_100mm_1573K (C), Pr10_25mm_1573K (D).

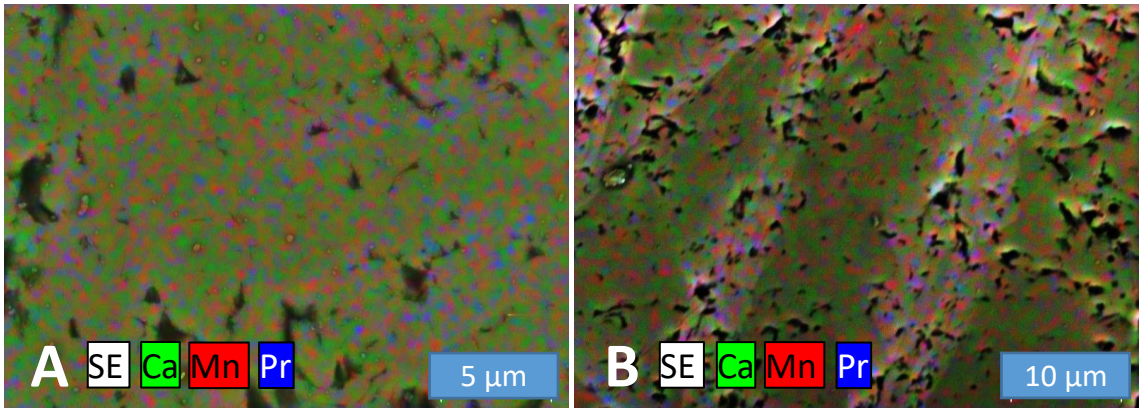

Figure 3.12 - EDS mapping results for the longitudinal section of the thermally treated fibres: Pr10_25mm_1573K (A) and Pr6_100mm_1573K (B).

Electrical conductivity

In accordance with the literature data (e.g. (Zhang, 2013) and references therein), electronic transport in donor-substituted manganites, like $Ca_{1-x}Pr_xMnO_3$, occurs via small polaron mechanism. The charge carriers are generated through compensation of excessive charge of the praseodymium cation as compared to calcium, by reduction of manganese cations.

This reaction, considered used precursors, can be represented as follows:

$$\frac{1}{6}xPr_6O_{11} + (1-x)CaCO_3 + MnO_2 \rightarrow xPr_{Ca}^{\bullet} + (1-x)Ca_{Ca}^{x} + x\mathrm{Mn}_{\mathrm{Mn}}^{'} + xMn_{Mn}^{x} + 3O_O^x + (1-x)CO_2(g) + \frac{5}{12}xO_2(g) \quad \text{Eq. 14}$$

In this way, the concentration of charge carriers and, consequently, the electrical conductivity are expected to increase with praseodymium concentration. This expectation is in agreement with the results on the electrical conductivity vs. temperature dependence, presented in Figure 3.13. All samples present metallic-like behaviour of the conductivity with the temperature, quite typical for perovskite donor-substituted calcium manganite (Zhang, 2013)(Wang, 2009)(Wang, 2016)(Park, 2009). Additional charge carriers can be generated by tetravalent Pr^{4+} substituting calcium this contribution was not taken into account in Eq. 14.

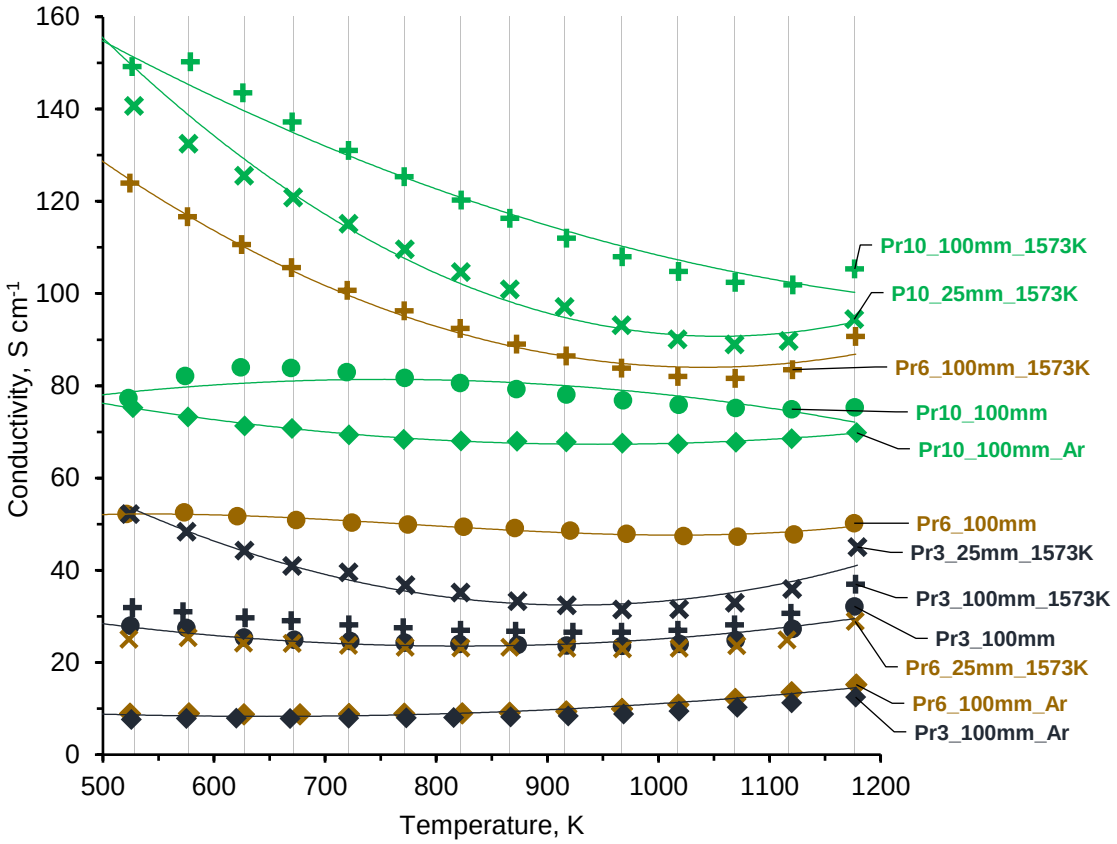

Figure 3.13 – Electrical conductivity, σ, as a function of temperature for all samples.

As follows from Fig. 3.13, the electrical conductivity is strongly dependent on praseodymium concentration. For (Pr,Ca)$MnO_{3-\delta}$ system, previous work suggests an increase of conductivity with substitution content up to a saturation value at 15% of concentration of the rare earth element content (Okamoto, 1991). Therefore, the lowest conductivity values are characteristic to the samples containing 3% mol. of praseodymium irrespectively of the processing conditions, in good agreement with the values between 7 to 50 S cm^{-1} observed in (Zhang, 2013). Higher values of conductivity were observed for samples with the higher praseodymium content, with attractive conductivities from 67 to 150 S cm^{-1}, again, showing tendencies in accordance with previous works (Zhang, 2013)(Cong, 2004). Highest value of 150 S cm^{-1} was observed for 10Pr_100mm_1573K sample at 579 K and 100 S cm^{-1} at 1070K.

While the praseodymium concentration dependence of the electrical conductivity in most cases holds the expected behaviour, the impact of the processing conditions demonstrates more complex trends. These trends, however, often show a good correlation with phase composition and microstructure of the samples.

In particular, the samples grown in Ar show the lowest conductivities, as of 7.6 S cm^{-1} at 526 K for 3Pr_100mm_Ar, compared to those processed under air. In accordance with the XRD results (Fig. 3.2) and combined SEM/EDS studies (Fig. 3.5 and 3.6), Ar-grown fibres possess the highest amount of phase inhomogeneities and impurities. Spinel-type $CaMn_2O_4$, Ruddlesden-Popper-type $Ca_3Mn_2O_7$ and brownmillerite-type $Ca_2Mn_2O_5$ phases offer significantly lower electrical conductivity cations as compared to $CaMnO_3$-based perovskite-type lattice (White, 2009)(Toyoda, 2011)(Molinari, 2014). Part of the praseodymium cations may also enter the crystal lattice of the above composition, effectively decreasing the donor-substitution level in the perovskite phase. Also, the presence of Pr-rich (Pr,Ca)$MnO_{3-\delta}$ may be even favourable for the conductivity based on the results presented in (Huang, 2002), the amount of this impurity is too low effective percolation. Lowest conductivity of around 7-8 S cm^{-1} at 526 K was measured for 3Pr_100mm_Ar sample. The samples grown in air and possessing lower amount of impurity phases show higher conductivity. This tendency is much more pronounced for thermally treated fibres, where re-equilibrium of the phase composition and corresponding minimal impurities content provide further enhancement of electrical transport. Highest electrical conductivity (Fig. 3.13) were observed for thermally treated $Ca_{0.90}Pr_{0.10}MnO_3$, grown at 25 and 100 mm h^{-1}. Pr6_100mm_1573K shows comparable conductivity values, while too low conductivity of Pr6_25mm_1573K is actually surprising. The microstructural studies (Fig. 3.11) suggest noticeably higher porosity for Pr6_25mm_1573K as compared to Pr6_100mm_1573K, but such porosity difference cannot fully justify the observed conductivity decrease. Additional studies are required to reveal the mechanisms of the behaviour.

Seebeck coefficient

In the case of hopping conduction mechanism, the Seebeck coefficient can be represented as follows (Leonidov, 2017):

$$S = -\frac{k_B}{|e|}\left(ln\frac{N_{av}}{n} + \frac{E_S}{k_B T}\right) \qquad \text{Eq. 15}$$

where k_B is Boltzmann´s constant, e is the electron charge, n is the charge carrier concentration, N_{av} is the number of sites available for carrier hopping and E_S is the activation energy. For negligible concentration of the hopping sites, the Seebeck coefficient is dominated by the second term, like for non-substituted $CaMnO_3$. In the case of (Pr,Ca)$MnO_{3-\delta}$, the substitution generates the sites available for electron hopping sites, and the first term of the Eq. 15 starts to determine the behaviour of the Seebeck coefficient. Fig. 3.14 presents the Seebeck coefficient of the studied materials as a function of temperature. The S values for all samples are negative, confirming that the electron carriers are dominant. The observed general increase in the Seebeck coefficient may be attributed to the increase of $N_{av}\, n^{-1}$ term on heating, in particular, due to disproportionation reaction 2 $Mn^{3+} \leftrightarrow Mn^{2+} + Mn^{4+}$ and corresponding decrease in the charge carrier concentration, which may take place even in the presence of donor substitution (Leonidov, 2017).

Since the Seebeck coefficient is inversely proportional to the carrier concentration, in terms of dependence on praseodymium content we expect opposite trends for S and electrical conductivity. Indeed, the samples with higher praseodymium content and higher conductivity (Fig. 3.13), in general demonstrate lower Seebeck conductivity (Fig. 3.14) and vice versa. However, processing conditions for the same substitution level impose more complex effects, which may include the contributions provided by impurity phases and corresponding deviations in the chemical composition of the perovskite phase. In opposite to electrical conductivity, the Seebeck coefficient is not directly affected by porosity; this may also affect the expected trends. Best observed absolute values of Seebeck coefficient correspond to 259 μV K^{-1} at 1120 K for Pr3_25mm_1573K. The literature data report 148 μV K^{-1} at 1080 K for $Ca_{0.9}Pr_{0.1}MnO_3$ (Choi, 2011) and 160 μV K^{-1} at 965 K for $Ca_{0.92}Pr_{0.08}MnO_3$ (Zhang, 2013).

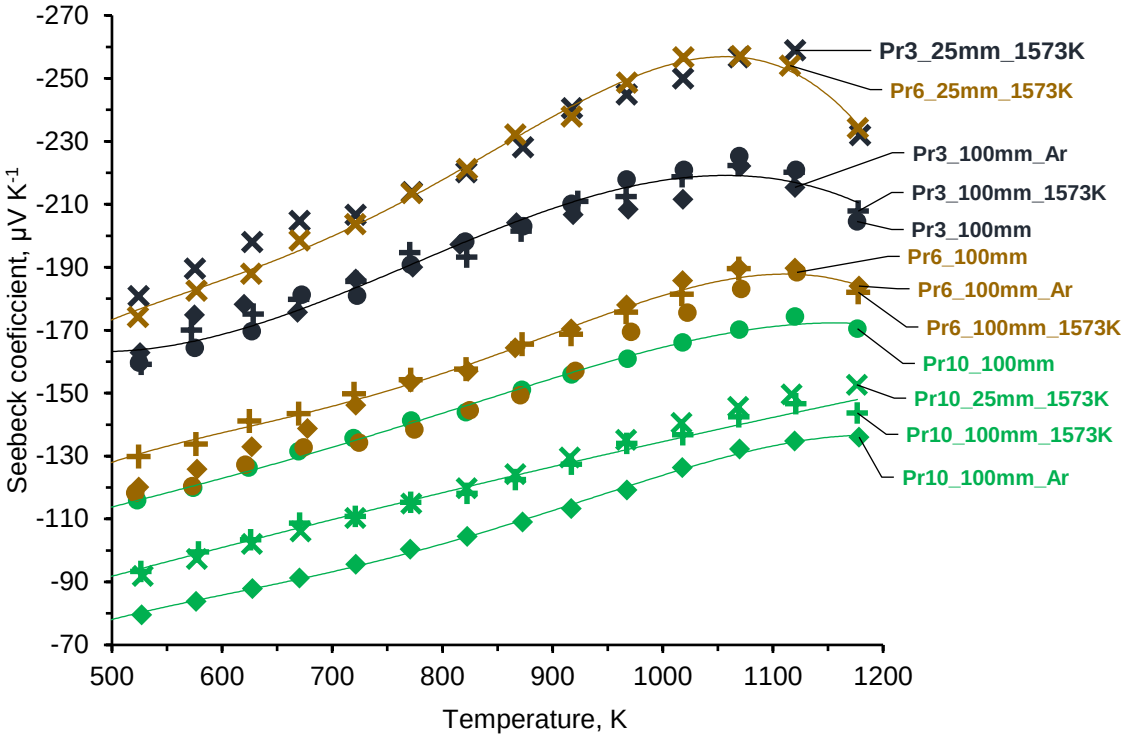

Figure 3.14 - Seebeck coefficient (S) as a function of temperature for all samples.

Thermoelectric performance

The values of power factor illustrate the cumulative effect provided by electrical conductivity and Seebeck coefficient on thermoelectric performance. The data presented in Figure 3.15 shows temperature dependence of the power factor ($S^2\sigma$). General increase of PF with temperature corresponds to the behaviour of *S*-*T* and σ-*T* curves previously discussed. As for conductivity and Seebeck coefficient, the power factor is sensitive to both substitution level and processing conditions. Presence of significant phase impurities in the samples grown in Ar results in lowest power factors. An interesting case is represented by $Ca_{0.9}Pr_{0.1}MnO_3$ composition, for which the PF values of samples grown in air are comparable irrespectively of LFZ or thermal treatment conditions. This situation was previously described in the Section 1.1.3 (Figure 1.4) and corresponds to the case when the substitution promotes too excessive concentration of the charge carries, and relatively high electrical conductivity is compensated by comparatively low absolute values of Seebeck coefficient. On the contrary, significant enhancement of the power factor by processing conditions is possible for $Ca_{0.94}Pr_{0.06}MnO_3$; this apparently corresponds to the PF maximum in Figure 3.15. The sample Pr6_100mm_1573K showed the highest power factor value of 303 µW m^{-1} k^{-2} at 1120 K. Works done on donor substituted calcium manganese type material report 252 µW m^{-1} k^{-2} at 1073 K (Kabir, 2014) for $Ca_{0.9}Yb_{0.1}MnO_3$,280 µW m^{-1} k^{-2} at 1073 K (Ohtaki, 1995) for $Ca_{0.9}Bi_{0.1}MnO_3$, 400 µW m^{-1} k^{-2} at 750 K (Kabir, 2015) for $Ca_{0.97}Bi_{0.03}MnO_3$. in the case of Pr-substituted calcium manganese prepared via standard ceramic route, the results suggest an ideal doping content of 15% to attain maximum electrical performance (Cong, 2004). Maximum power factor of 243 µW m^{-1} k^{-2} at 1180 (Zhang, 2013). 400 and 342 µW m^{-1} k^{-2} at 1132 K (Choi, 2011)(Zhang, 2013) for $Ca_{0.9}Pr_{0.1}MnO_3$. Still, if compared to the results above, the performance achived in present work for $Ca_{0.94}Pr_{0.06}MnO_3$, grown at 100 mm h^{-1} in air and post-processed at 1553 K, is very promising and shows the potential for further improvement. This also holds even for Seebeck coefficient. Corresponding charge carrier mobility studies along with the charge carrier relevant mechanisms in order to define further strategies for processing these materials to impart even better thermoelectric properties.

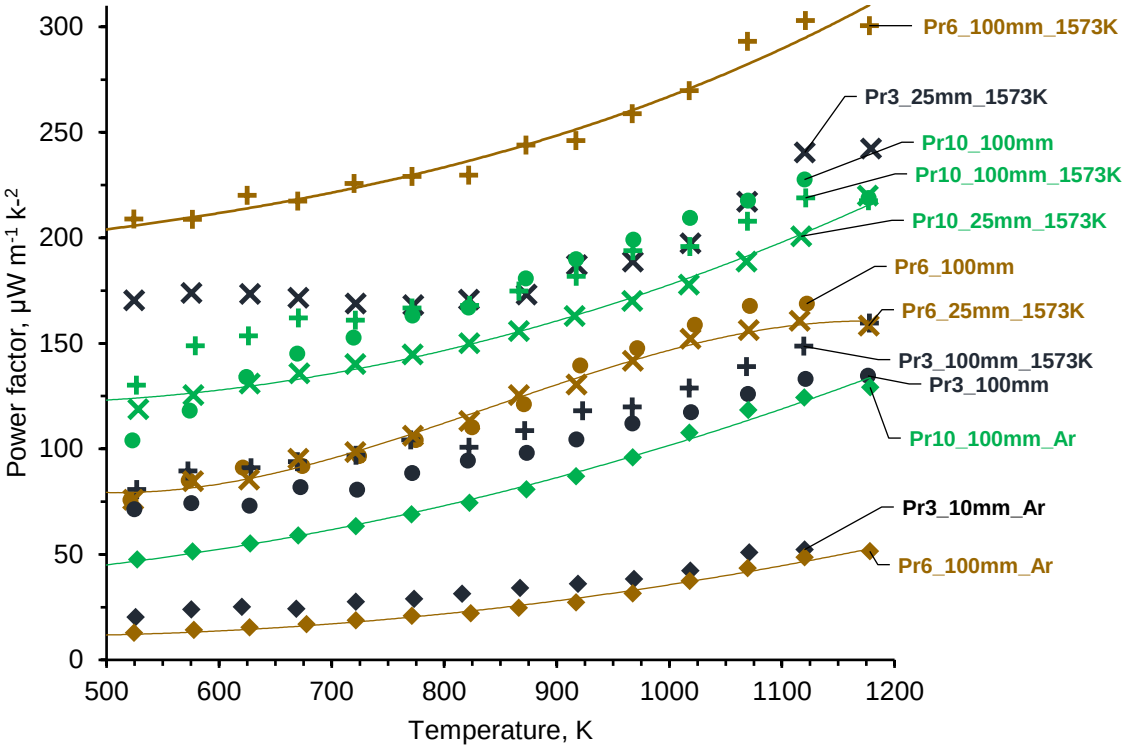

Figure 3.15 – Power factor (PF) as a function of temperature for all samples.

3.5 STABILITY OF THERMOELECTRIC PERFORMANCE

As it was shown above, due to strongly non-equilibrium processing conditions, LFZ technique induces significant amount of secondary phases in the samples grown at various pulling rates and atmospheres, and promotes the appearance of various specific microstructural features like core-shell structures. During operation under prospective high-temperature conditions a re-equilibration of the fibre composition can take place, leading to the changes in performance. Figure 3.16 shows time dependencies of key thermoelectric properties at high temperature.

These results indicate that the most significant changes in the case of as-grown fibres are associated with the electrical conductivity. This is due to the fact that the electrical conductivity of perovskite-type phase is essentially higher than that for observed impurities (White, 2009)(Toyoda, 2011)(Molinari, 2014). Corresponding changes in Seebeck coefficient are rather moderate. For all as-grown fibres the power factor increases with time, highlighting that, for the selected compositions range, an additional thermal treatment after LFZ processing is needed in order to attain maximum thermoelectric performance. As an example, only minor changes in electrical conductivity and Seebeck coefficient with time were observed for thermally-treated Pr10_100mm_1573K sample; these values are within experimental error range of the measurements. This is also confirmed by generally higher performance of the thermally-treated fibres as compared to as-grown (Figs 3.13, 3.14 and 3.15). Although the obtained guidelines do not necessarily mean that an additional thermal treatment is always required to obtain maximum thermoelectric performance in LFZ processed fibres, this may have some technological implications.

Firstly, the formation of desired phases could be facilitated by powder pre-preparation procedure, where the perovskite phase is already formed. This, however, reduces the advantage of LFZ processing for thermoelectric oxides as one-step process.

Secondly, re-equilibration may be performed by second step of laser processing, when, after growth, the sample again passes through laser zone with less power to avoid melting while facilitating further reactions. Finally, there are still more possibilities to adjust LFZ process moving to lower growth rates, since above it was demonstrated that the samples processes at lower rate of 25 mm h^{-1} show better phase compositions compared to 100 mm h^{-1}. These directions constitute promising approaches for future work.

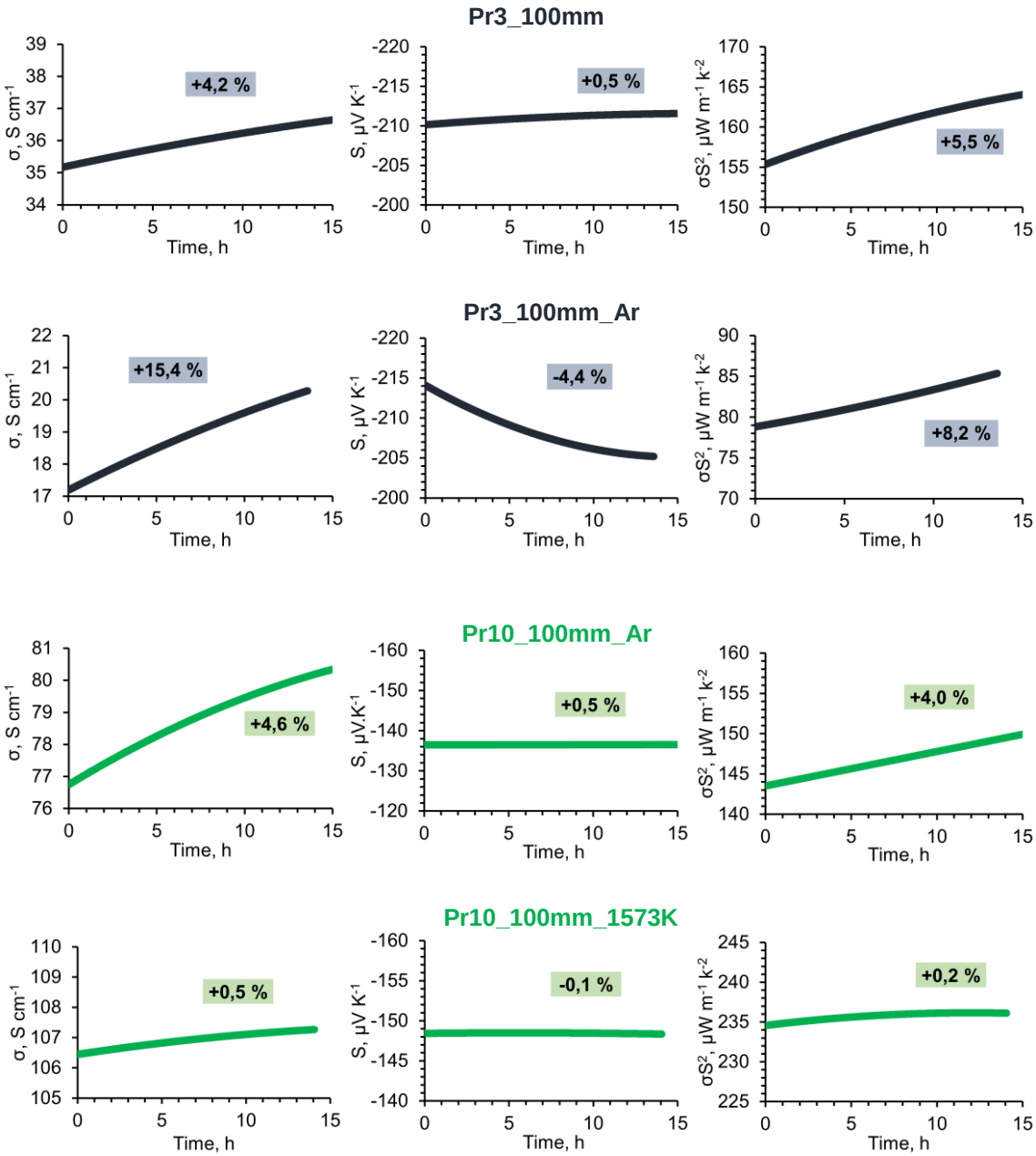

Figure 3.16 - Electrical conductivity, Seebeck coefficient and power factor as a function of time at 1173 K. The values in % illustrate the extent of evolution of the thermoelectric properties for each composition.

CHAPTER 4

CONCLUSIONS AND FUTURE WORK

4 CONCLUSIONS AND FUTURE WORK

Possibilities for processing calcium manganite-based thermoelectric materials using a non-conventional laser floating zone processing technique were assessed. Praseodymium-substituted $Ca_{1-x}Pr_xMnO_3$ (x=0.03, 0.06, 0.1) was selected as a model system, given by promising thermoelectric properties already observed for these compositions prepared by standard ceramic technology.

As a first step, optimization of the powder processing and LFZ conditions was conducted taking into account specific material characteristics and behaviour. This was done in order to produce mechanically strong fibres with appropriate geometrical shape suitable for thermoelectric characterization. Pulling rates along with growth atmosphere were varied seeking best TE properties. Selected pulling rates corresponded to 200 mm h^{-1}, 100 mm h^{-1} and 25 mm h^{-1}, while the atmospheres of air, argon or vacuum were applied. Fast pulling rates (200 mm h^{-1}) produced inhomogeneous fibres, which were not appropriate for electrical characterization both due to irregular geometric shape and possible severe phase inhomogeneities. Growth in vacuum conditions was also unsuccessful due to appearance of instabilities in the molten zone precluding the formation of uniform fibres. Growth in air and argon atmospheres at pulling rate of 100 mm h^{-1} resulted in formation of major perovskite phase, along with secondary $CaMn_2O_4$, $Ca_3Mn_2O_7$, $Ca_2Mn_2O_5$, and praseodymium-rich $PrMnO_3$ phases, and specific microstructures including dendritic regions and core-shells, with potential impact on electronic and thermal transport properties. Slow pulling rate of 25 mm h^{-1} favoured the formation of desired perovskite-type phase, possessing attractive thermoelectric properties. Post-processing at high temperature (1573 K for 10h) in air atmosphere was employed to facilitate the equilibration of the phase composition of prepared fibres and to improve their mechanical strength. This treatment resulted in elimination of $Ca_3Mn_2O_7$ and $Ca_2Mn_2O_5$ secondary phases and favourable microstructural evolution.

Measurements of the electrical conductivity and Seebeck coefficient were performed in air under stepwise cooling from 1200 K to 500 K. The values of the power factor were calculated from these data. Electrical conductivity was enhanced, as expected, with increase of praseodymium content, and also by post-processing at high temperatures. The changes in electrical conductivity depending on the processing conditions are correlated with the phase composition and microstructural evolution. The effects of processing conditions on Seebeck coefficient are more complex and include the contributions provided by impurity phases and corresponding deviations in the chemical composition of the perovskite phase. In terms of the power factor, the best performance achieved in present work corresponded to $Ca_{0.94}Pr_{0.06}MnO_3$ material grown at 100 mm h^{-1} in air and post-processed at 1573 K, with a PF value of 303 μW m^{-1} K^{-2} at 1120 K.

Long-term recordings of the electrical conductivity and Seebeck coefficient was performed to evaluate the stability of the fibres in terms of thermoelectric performance, also taking into account prospective operation conditions. Results showed an increase of power factor under high temperatures for as-grown fibres mainly due to increase of electrical conductivity, promoted by evolution of phase composition towards $CaMnO_3$ perovskite. These results also justify the necessity for post-thermal treatment after LFZ processing in order to attain maximum thermoelectric performance when operating at high temperatures of 1173 K. The laser floating zone technique can be used for producing thermoelectric materials. However, optimal growth parameters still remain a challenge when seeking the best phase composition. Still, the results obtained in this work give some guidelines for future research directions. An improvement of the phase composition towards perovskite and correspondingly higher thermoelectric performance may be attained by applying lower growth rates, together with oxygen atmosphere, which is expected to supress secondary phases like $CaMn_2O_4$ by favouring Mn^{4+}.

Further optimization can be done via application of second step of low-power laser processing (like laser sintering) avoiding necessity for post-thermal treatment, especially at slow pulling rates. Thus, maintaining the preferential phase composition and adding conditions for the

processing of mechanically strong fibres. Measurements of the thermal conductivity are essential for better understanding of the changes imposed by the pulling rate on structural features, affecting the thermal transport. Also, the addition of the substituent in comparison with their influence on the electrical conductivity. Studies on the three quantities of the figure of merit are needed for full comprehension of the unique features imposed by the laser floating zone technique. Also, *ZT* value calculation would help to evaluate the thermoelectric potential of this material.

IV. REFERENCES

(Abe, 2000) - Abe, T. (2000). Formation mechanism of grown-in defects in CZ silicon crystals based on thermal gradients measured by thermocouples near growth interfaces. *Materials Science and Engineering B: Solid-State Materials for Advanced Technology*, *73*(1), 16–29. https://doi.org/10.1016/S0921-5107(99)00428-6

Alam, H., & Ramakrishna, S. (2013). A review on the enhancement of figure of merit from bulk to nano-thermoelectric materials. *Nano Energy*, *2*(2), 190–212. https://doi.org/10.1016/j.nanoen.2012.10.005

Bakken, E., Norby, T., & Stølen, S. (2005). Nonstoichiometry and reductive decomposition of CaMnO3-δ. *Solid State Ionics*, *176*(1–2), 217–223. https://doi.org/10.1016/j.ssi.2004.07.001

Bentien, A., Christensen, M., Bryan, J. D., Sanchez, A., Paschen, S., Steglich, F., … Iversen, B. B. (2004). Thermal conductivity of thermoelectric clathrates. *Physical Review B - Condensed Matter and Materials Physics*, *69*(4), 045107. https://doi.org/10.1103/PhysRevB.69.045107

Bentien, A., Pacheco, V., Paschen, S., Grin, Y., & Steglich, F. (2005). Transport properties of composition tuned a- and b-Eu8Ga16−xGe30+x. *Phys. Rev. B*, *71*(16), 165206/1-12. Retrieved from https://link.aps.org/doi/10.1103/PhysRevB.71.165206

Billi, D. (2012). *Anhydrobiotic rock-inhabiting cyanobacteria: Potential for astrobiology and biotechnology*. *Adaption of Microbial Life to Environmental Extremes: Novel Research Results and Application*. Universität Augsburg. https://doi.org/10.1007/978-3-211-99691-1_6

Biswas, K., He, J., Blum, I. D., Wu, C.-I., Hogan, T. P., Seidman, D. N., … Kanatzidis, M. G. (2012). High-Performance Bulk Thermoelectrics with All-Scale Hierarchical Architectures. *Nature*, *489*, 414. Retrieved from http://dx.doi.org/10.1038/nature11439

Bocher, L., Aguirre, M. H., Logvinovich, D., Shkabko, A., Robert, R., Trottmann, M., & Weidenkaff, A. (2008). CaMn1-x NbxO3 (x ≤ 0.08) perovskite-type phases as promising new high-temperature n-type thermoelectric materials. *Inorganic Chemistry*, *47*(18), 8077–8085. https://doi.org/10.1021/ic800463s

Bocher, L., Aguirre, M. H., Robert, R., Logvinovich, D., Bakardjieva, S., Hejtmanek, J., & Weidenkaff, A. (2009). High-temperature stability, structure and thermoelectric properties of CaMn1 - xNbxO3phases. *Acta Materialia*, *57*(19), 5667–5680. https://doi.org/10.1016/j.actamat.2009.07.062

Caillat, T., Fleurial, J.-P., & Borshchevsky, A. (1997). Preparation and thermoelectric properties of semiconducting Zn4Sb3. *Journal of Physics and Chemistry of Solids*, *58*(7), 1119–1125. https://doi.org/10.1016/S0022-3697(96)00228-4

Carvalho, R. G., Pires, M. S., Fernandes, A., Silva, R., & Costa, F. (2013). *Directionally solidified eutectic and off-eutectic mullite–zirconia fibres*. *Journal of the European Ceramic Society* (Vol. 33). https://doi.org/10.1016/j.jeurceramsoc.2012.09.032

Celorrio, V., Calvillo, L., Dann, E., Granozzi, G., Aguadero, A., Kramer, D., … Fermín, D. J. (2016). Oxygen reduction reaction at LaxCa1-xMnO3nanostructures: Interplay between A-site segregation and B-site valency. *Catalysis Science and Technology*, *6*(19), 7231–7238. https://doi.org/10.1039/c6cy01105e

Chester, G. V, & Thellung, A. (1961). The Law of Wiedemann and Franz. *Proceedings of the Physical Society*, *77*(5), 1005–1013. https://doi.org/10.1088/0370-1328/77/5/309

Choi, S.-M., Lim, C.-H., & Seo, W.-S. (2011). Thermoelectric Properties of the Ca1−x R x MnO3 Perovskite System (R: Pr, Nd, Sm) for High-Temperature Applications. *Journal of Electronic Materials*, *40*(5), 551–556. https://doi.org/10.1007/s11664-010-1446-3

Christensen, M., Snyder, G. J., & Iversen, B. B. (2006). High temperature thermoelectric

properties of Czochralski-pulled Ba8Ga16Ge30. In *2006 25th International Conference on Thermoelectrics* (pp. 40–43). https://doi.org/10.1109/ICT.2006.331265

Cong, B. T., Tsuji, T., Thao, P. X., Thanh, P. Q., & Yamamura, Y. (2004). High-temperature thermoelectric properties of Ca1-xPrxMnO3-δ(0≤x<1). *Physica B: Condensed Matter*, *352*(1–4), 18–23. https://doi.org/10.1016/j.physb.2004.06.033

Costa, F. M., Silva, R. F., & Vieira, J. M. (2001). Diffusion phenomena and crystallization path during the growth of LFZ Bi-Sr-Ca-Cu-O superconducting fibres. *Superconductor Science and Technology*, *14*(11), 910–920. https://doi.org/10.1088/0953-2048/14/11/305

Costa FM, Carrasco FG, Silva RF, V. J. (2005). High Tc Superconducting Fibers Processed by Conventional and electrical Assisted Laser Floating Zone. In P. S. Lewis (Ed.), *Perspectives on Superconductivity Research* (pp. 35–59). Nova Science Publishers, Inc.

Date, A., Date, A., Dixon, C., & Akbarzadeh, A. (2014). Progress of thermoelectric power generation systems: Prospect for small to medium scale power generation. *Renewable and Sustainable Energy Reviews*, *33*, 371–381. https://doi.org/10.1016/j.rser.2014.01.081

Dyck, J. S., Chen, W., Uher, C., Chen, L., Tang, X., & Hirai, T. (2002). Thermoelectric properties of the n-type filled skutterudite Ba0.3Co4Sb12 doped with Ni. *Journal of Applied Physics*, *91*(6), 3698–3705. https://doi.org/10.1063/1.1450036

Ewert, M. K. (1998). Terrestrial and aerospace solar heat pump and refrigerator development: Past, present and future. In *International Solar Energy Conference* (pp. 375–381). Albuquerque.

Fergus, J. W. (2012). Oxide materials for high temperature thermoelectric energy conversion. *Journal of the European Ceramic Society*, *32*(3), 525–540. https://doi.org/10.1016/j.jeurceramsoc.2011.10.007

Ferreira, N. M., Costa, F. M., Kovalevsky, A. V., Madre, M. A., Torres, M. A., Diez, J. C., & Sotelo, A. (2018). New environmentally friendly Ba-Fe-O thermoelectric material by flexible laser floating zone processing. *Scripta Materialia*, *145*, 54–57. https://doi.org/10.1016/j.scriptamat.2017.10.011

Ferreira, N. M., Ferro, M. C., Valente, M. A., Frade, J. R., Costa, F. M., & Kovalevsky, A. V. (2018). Unusual redox behaviour of the magnetite/hematite core-shell structures processed by the laser floating zone method. *Dalton Transactions*, *47*(16), 5646–5651. https://doi.org/10.1039/c7dt04775d

Ferreira, N. M., Kovalevsky, A., Valente, M. A., Costa, F. M., & Frade, J. (2013). Magnetite/hematite core/shell fibres grown by laser floating zone method. In *Applied Surface Science* (Vol. 278, pp. 203–206). https://doi.org/10.1016/j.apsusc.2013.01.108

Ferreira, N. M., Rasekh, S., Costa, F. M., Madre, M. A., Sotelo, A., Diez, J. C., & Torres, M. A. (2012). New method to improve the grain alignment and performance of thermoelectric ceramics. *Materials Letters*, *83*, 144–147. https://doi.org/10.1016/j.matlet.2012.05.131

Ge, Z.-H., Song, D., Chong, X., Zheng, F., Jin, L., Qian, X., … Zhao, L.-D. (2017). Boosting the Thermoelectric Performance of (Na,K)-Codoped Polycrystalline SnSe by Synergistic Tailoring of the Band Structure and Atomic-Scale Defect Phonon Scattering. *Journal of the American Chemical Society*, *139*(28), 9714–9720. https://doi.org/10.1021/jacs.7b05339

Guéguen, A., Poudeu, P. F. P., Li, C. P., Moses, S., Uher, C., He, J., … Kanatzidis, M. G. (2009). Thermoelectric properties and nanostructuring in the p-type materials NaPb18-xSnxMTe20(M = Sb, Bi). *Chemistry of Materials*, *21*(8), 1683–1694. https://doi.org/10.1021/cm803519p

Han, X., Zhang, T., Du, J., Cheng, F., & Chen, J. (2013). Porous calcium-manganese oxide microspheres for electrocatalytic oxygen reduction with high activity. *Chemical Science*, *4*(1), 368–376. https://doi.org/10.1039/c2sc21475j

He, Y., Day, T., Zhang, T., Liu, H., Shi, X., Chen, L., & Snyder, G. J. (2014). High thermoelectric performance in non-toxic earth-abundant copper sulfide. *Advanced Materials*, *26*(23),

3974–3978. https://doi.org/10.1002/adma.201400515

Heremans, J. P., Wiendlocha, B., & Chamoire, A. M. (2012). Resonant levels in bulk thermoelectric semiconductors. *Energy and Environmental Science*, *5*(2), 5510–5530. https://doi.org/10.1039/c1ee02612g

Huang, X., Pei, L., Liu, Z., Lu, Z., Sui, Y., Qian, Z., & Su, W. (2002). A study on PrMnO3-based perovskite oxides used in SOFC cathodes. *Journal of Alloys and Compounds*, *345*(1–2), 265–270. https://doi.org/10.1016/S0925-8388(02)00411-5

Kabir, R., Tian, R., Zhang, T., Donelson, R., Tan, T. T., & Li, S. (2015). Role of Bi doping in thermoelectric properties of CaMnO3. *Journal of Alloys and Compounds*, *628*, 347–351. https://doi.org/10.1016/j.jallcom.2014.12.141

Kabir, R., Wang, D., Zhang, T., Tian, R., Donelson, R., Teck Tan, T., & Li, S. (2014). Tunable thermoelectric properties of Ca0.9Yb0.1MnO3through controlling the particle size via ball mill processing. *Ceramics International*, *40*(PB), 16701–16706. https://doi.org/10.1016/j.ceramint.2014.08.033

Kim, J.-H., Okamoto, N. L., Kishida, K., Tanaka, K., & Inui, H. (2006). High thermoelectric performance of type-III clathrate compounds of the Ba–Ge–Ga system. *Acta Materialia*, *54*(8), 2057–2062. https://doi.org/10.1016/J.ACTAMAT.2005.12.032

Kinemuchi, Y., Mikami, M., Terasaki, I., & Shin, W. (2016). Rapid synthesis of thermoelectric compounds by laser melting. *Materials and Design*. https://doi.org/10.1016/j.matdes.2016.05.093

Koc, R., & Anderson, H. U. (1992). Electrical conductivity and Seebeck coefficient of (La, Ca)(Cr, Co)O3. *Journal of Materials Science*, *27*(20), 5477–5482. https://doi.org/10.1007/BF00541609

Koumoto, K., Funahashi, R., Guilmeau, E., Miyazaki, Y., Weidenkaff, A., Wang, Y., & Wan, C. (2013). Thermoelectric ceramics for energy harvesting. *Journal of the American Ceramic Society*, *96*(1), 1–23. https://doi.org/10.1111/jace.12076

Koumoto, K., Terasaki, I., & Funahashi, R. (2006). Complex Oxide Materials for Potential Thermoelectric Applications. *MRS Bulletin*, *31*(3), 206–210. https://doi.org/DOI: 10.1557/mrs2006.46

Lan, Y., Minnich, A. J., Chen, G., & Ren, Z. (2010). Enhancement of Thermoelectric Figure-of-Merit by a Bulk Nanostructuring Approach. *Advanced Functional Materials*, *20*(3), 357–376. https://doi.org/10.1002/adfm.200901512

Leonidov, I. A., Konstantinova, E. I., Patrakeev, M. V., Markov, A. A., & Kozhevnikov, V. L. (2017). Seebeck coefficient of Ca1–xPrxMnO3–δ paramagnetic manganites. *Inorganic Materials*, *53*(6), 583–588. https://doi.org/10.1134/S0020168517060097

Liu, H., Shi, X., Xu, F., Zhang, L., Zhang, W., Chen, L., … Snyder Jeffrey, G. (2012). Copper ion liquid-like thermoelectrics. *Nature Materials*, *11*(5), 422–425. https://doi.org/10.1038/nmat3273

Liu, H., Yuan, X., Lu, P., Shi, X., Xu, F., He, Y., … Uher, C. (2013). Ultrahigh Thermoelectric Performance by Electron and Phonon Critical Scattering in Cu Se I. *Advanced Materials*, *25*(45), 6607–6612. https://doi.org/10.1002/adma.201302660

Liu, W., Tan, X., Yin, K., Liu, H., Tang, X., Shi, J., … Uher, C. (2012). Convergence of conduction bands as a means of enhancing thermoelectric performance of n-type Mg2Si1-xSnxsolid solutions. *Physical Review Letters*, *108*(16), 166601. https://doi.org/10.1103/PhysRevLett.108.166601

Luo, J., You, L., Zhang, J., Guo, K., Zhu, H., Gu, L., … Zhang, W. (2017). Enhanced Average Thermoelectric Figure of Merit of the PbTe–SrTe–MnTe Alloy. *ACS Applied Materials & Interfaces*, *9*(10), 8729–8736. https://doi.org/10.1021/acsami.6b16060

Mazur, N. M. (2015). *Microstructural design of CaMnO3 and its thermoelectric proprieties .*

Norwegian University of Science and Technology.

Mishra, A., & Bhattacharjee, S. (2017). Effect of A- or B-site doping of perovskite calcium manganite on structure, resistivity, and thermoelectric properties. *Journal of the American Ceramic Society*, *100*(10), 4945–4953. https://doi.org/10.1111/jace.15015

Molinari, M., Tompsett, D. A., Parker, S. C., Azough, F., & Freer, R. (2014). Structural, electronic and thermoelectric behaviour of CaMnO3and CaMnO(3-δ). *Journal of Materials Chemistry A*, *2*(34), 14109–14117. https://doi.org/10.1039/c4ta01514b

Naz, N., Rizvi, S. K., & Sadiq, Z. (2017). Assessment of thyroid hormone levels & thyroid disorders: A case study from Gujranwala, Pakistan. *Pakistan Journal of Pharmaceutical Sciences*, *30*(4), 1245–1249. https://doi.org/10.1126/science.1159725

Nuno Rosado Neves. (2017). *Processamento a laser de materiais termoelétricos e suas propriedades*. University of Aveiro.

Ohtaki, M. (2011). Recent aspects of oxide thermoelectric materials for power generation from mid-to-high temperature heat source. *Journal of the Ceramic Society of Japan*, *119*(1395), 770–775. https://doi.org/10.2109/jcersj2.119.770

Ohtaki, M., Koga, H., Tokunaga, T., Eguchi, K., & Arai, H. (1995). Electrical transport properties and high-temperature thermoelectric performance of (Ca0.9M0.1)MnO3 (M = Y, La, Ce, Sm, In, Sn, Sb, Pb, Bi). *Journal of Solid State Chemistry*. https://doi.org/10.1006/jssc.1995.1384

Ohtaki, M., Tsubota, T., Eguchi, K., & Arai, H. (1996). High-temperature thermoelectric properties of (Zn1−xAlx)O. *Journal of Applied Physics*, *79*(3), 1816–1818. https://doi.org/10.1063/1.360976

Okamoto, H. (1991). Phase diagram updates. *Journal of Phase Equilibria*, *12*(6), 696. https://doi.org/10.1007/BF02649933

Park, J. W., Kwak, D. H., Yoon, S. H., & Choi, S. C. (2009). Thermoelectric properties of Bi, Nb co-substituted CaMnO3at high temperature. *Journal of Alloys and Compounds*, *487*(1–2), 550–555. https://doi.org/10.1016/j.jallcom.2009.08.012

Pei, Y., Shi, X., LaLonde, A., Wang, H., Chen, L., & Snyder, G. J. (2011). Convergence of electronic bands for high performance bulk thermoelectrics. *Nature*, *473*, 66. Retrieved from http://dx.doi.org/10.1038/nature09996

Pei, Y., Wang, H., & Snyder, G. J. (2012). Band engineering of thermoelectric materials. *Advanced Materials*, *24*(46), 6125–6135. https://doi.org/10.1002/adma.201202919

Pi, L., Hébert, S., Martin, C., Maignan, A., & Raveau, B. (2003). Comparison of CaMn1-xRuxO3 and CaMn1-yMoyO3 perovskites. *Physical Review B - Condensed Matter and Materials Physics*, *67*(2), 244301–244307. https://doi.org/10.1103/PhysRevB.67.024430

Poudel, B., Hao, Q., Ma, Y., Lan, Y., Minnich, A., Yu, B., … Ren, Z. (2008). High-Thermoelectric Performance of Nanostructured Bismuth Antimony Telluride Bulk Alloys. *Science*, *1871*(May), 634–639. Retrieved from http://science.sciencemag.org/content/320/5876/634.abstract

Puyet, M., Dauscher, A., Lenoir, B., Dehmas, M., Stiewe, C., Müller, E., & Hejtmanek, J. (2005). Beneficial effect of Ni substitution on the thermoelectric properties in partially filled CayCo4−xNixSb12 skutterudites. *Journal of Applied Physics*, *97*(8), 83712. https://doi.org/10.1063/1.1868083

Puyet, M., Lenoir, B., Dauscher, A., Dehmas, M., Stiewe, C., & Müller, E. (2004). High temperature transport properties of partially filled CaxCo4Sb12 skutterudites. *Journal of Applied Physics*, *95*(9), 4852–4855. https://doi.org/10.1063/1.1688463

Rasekh, S., Costa, F. M., Ferreira, N. M., Torres, M. A., Madre, M. A., Diez, J. C., & Sotelo, A. (2015). Use of laser technology to produce high thermoelectric performances in Bi2Sr2Co1.8Ox. *Materials and Design*, *75*, 143–148.

https://doi.org/10.1016/j.matdes.2015.03.005

Ritzert, F., Westfall, L., & Center, L. (1996). Laser-heated floating zone production of single-crystal fibers. *NASA Technical Memorandum*, *4732*(January).

Saidur, R., Rezaei, M., Muzammil, W. K., Hassan, M. H., Paria, S., & Hasanuzzaman, M. (2012). Technologies to recover exhaust heat from internal combustion engines. *Renewable and Sustainable Energy Reviews*. Elsevier. https://doi.org/10.1016/j.rser.2012.05.018

Sakurada, S., & Shutoh, N. (2005). Effect of Ti substitution on the thermoelectric properties of (Zr,Hf)NiSn half-Heusler compounds. *Applied Physics Letters*, *86*(8), 82105. https://doi.org/10.1063/1.1868063

Scheel, H. J. (2003, February 19). The Development of Crystal Growth Technology. *Crystal Growth Technology*. https://doi.org/10.1002/chin.200542244

Seebeck, T. J. (1826). Ueber die magnetische Polarisation der Metalle und Erze durch Temperatur-Differenz. *Annalen Der Physik*, *82*(1), 1–20. https://doi.org/10.1002/andp.18260820202

Shannon, R. D. (1976). Revised effective ionic radii and systematic studies of interatomic distances in halides and chalcogenides. *Acta Crystallographica Section A*, *32*(5), 751–767. https://doi.org/10.1107/S0567739476001551

Sharp, J. W., Sales, B. C., Mandrus, D. G., & Chakoumakos, B. C. (1999). Thermoelectric properties of Tl2SnTe5 and Tl2GeTe5. *Applied Physics Letters*, *74*(25), 3794–3796. https://doi.org/10.1063/1.124182

Sodeoka, R. F. and I. M. and H. I. and T. T. and U. M. and S. (2000). An Oxide Single Crystal with High Thermoelectric Performance in Air. *Japanese Journal of Applied Physics*, *39*(11B), L1127. Retrieved from http://stacks.iop.org/1347-4065/39/i=11B/a=L1127

Sootsman, J. R., Chung, D. Y., & Kanatzidis, M. G. (2009). New and old concepts in thermoelectric materials. *Angewandte Chemie - International Edition*, *48*(46), 8616–8639. https://doi.org/10.1002/anie.200900598

Sotelo, A., Guilmeau, E., Madre, M. A., Marinel, S., Diez, J. C., & Prevel, M. (2007). Fabrication and properties of textured Bi-based cobaltite thermoelectric rods by zone melting. *Journal of the European Ceramic Society*, *27*(13–15), 3697–3700. https://doi.org/10.1016/j.jeurceramsoc.2007.02.020

Tang, X., Xie, W., Li, H., Zhao, W., Zhang, Q., & Niino, M. (2007). Preparation and thermoelectric transport properties of high-performance p-type Bi2Te3 with layered nanostructure. *Applied Physics Letters*, *90*(1), 12102. https://doi.org/10.1063/1.2425007

Tang, X., Zhang, Q., Chen, L., Goto, T., & Hirai, T. (2005). Synthesis and thermoelectric properties of p-type- and n-type-filled skutterudite RyMxCo4−xSb12(R:Ce,Ba,Y;M:Fe,Ni). *Journal of Applied Physics*, *97*(9), 93712. https://doi.org/10.1063/1.1888048

Tani, H. K. and R. A. and T. (2004). Thermoelectric Properties of Highly Textured Ca-Doped (ZnO) m In 2 O 3 Ceramics. *Japanese Journal of Applied Physics*, *43*(10R), 7133. Retrieved from http://stacks.iop.org/1347-4065/43/i=10R/a=7133

Thomson, W. (1853). On the Dynamical Theory of Heat. *Transactions of the Royal Society of Edinburgh*, *20*(02), 261–288. https://doi.org/10.1017/S0080456800033172

Toyoda, T., Sasaki, N., Shimada, K., Okube, M., & Sasaki, S. (2011). High-temperature thermoelectric property of layered La2-2xCa1+2xMn2O7Manganites (0.75 ≤ x ≤ 1.0). *Japanese Journal of Applied Physics*, *50*(4 PART 1). https://doi.org/10.1143/JJAP.50.041101

Villars, P., & Cenzual, K. (Eds.). (n.d.). CaMnO3 Crystal Structure: Datasheet from “PAULING FILE Multinaries Edition – 2012” in SpringerMaterials (https://materials.springer.com/isp/crystallographic/docs/sd_1403122). Springer-Verlag

Berlin Heidelberg & Material Phases Data System (MPDS), Switzerland & National Institute for Materials Science (NIMS), Japan. Retrieved from https://materials.springer.com/isp/crystallographic/docs/sd_1403122

Vining, C. B. (2009). An inconvenient truth about thermoelectrics TL - 8. *Nature Materials*, *8 VN-re*(2), 83–85. https://doi.org/10.1038/nmat2361

Wang, H., Su, W., Liu, J., & Wang, C. (2016). Recent development of n-type perovskite thermoelectrics. *Journal of Materiomics*, *2*(3), 225–236. https://doi.org/10.1016/j.jmat.2016.06.005

Wang, Y., Sui, Y., Cheng, J., Wang, X., Lu, Z., & Su, W. (2009a). High temperature metal-insulator transition induced by rare-earth doping in perovskite camno3. *Journal of Physical Chemistry C*, *113*(28), 12509–12516. https://doi.org/10.1021/jp809049s

Wang, Y., Sui, Y., Cheng, J., Wang, X., Lu, Z., & Su, W. (2009b). High temperature metal-insulator transition induced by rare-earth doping in perovskite CaMnO3. *Journal of Physical Chemistry C*, *113*(28), 12509–12516. https://doi.org/10.1021/jp809049s

Wang, Y., Sui, Y., Wang, X., Su, W., Liu, X., & Fan, H. J. (2010). Thermal conductivity of electron-doped CaMnO3perovskites: Local lattice distortions and optical phonon thermal excitation. *Acta Materialia*, *58*(19), 6306–6316. https://doi.org/10.1016/j.actamat.2010.07.052

White, B. D., Souza, J. A., Chiorescu, C., Neumeier, J. J., & Cohn, J. L. (2009). Magnetic, transport, and thermodynamic properties of CaMn2 O4 single crystals. *Physical Review B - Condensed Matter and Materials Physics*, *79*(10), 1–9. https://doi.org/10.1103/PhysRevB.79.104427

Wölfing, B., Kloc, C., Teubner, J., & Bucher, E. (2001). High performance thermoelectric Tl9BiTe6 with an extremely low thermal conductivity. *Physical Review Letters*, *86*(19), 4350–4353. https://doi.org/10.1103/PhysRevLett.86.4350

Wood, C. (1984). High-temperature thermoelectric energy conversion-II. Materials survey. *Energy Conversion and Management*, *24*(4), 331–343. https://doi.org/10.1016/0196-8904(84)90013-X

Wood, C. (1988). Materials for thermoelectric energy conversion. *Reports on Progress in Physics*, *51*(4), 459–539. https://doi.org/10.1088/0034-4885/51/4/001

Xi, L., Yang, J., Wu, L., Yang, J., & Zhang, W. (2016). Band engineering and rational design of high-performance thermoelectric materials by first-principles. *Journal of Materiomics*. https://doi.org/10.1016/j.jmat.2016.05.004

Xu, G., Funahashi, R., Pu, Q., Liu, B., Tao, R., Wang, G., & Ding, Z. (2004). High-temperature transport properties of Nb and Ta substituted CaMnO3system. *Solid State Ionics*, *171*(1–2), 147–151. https://doi.org/10.1016/S0167-2738(03)00108-5

Yang, J., Meisner, G. P., & Chen, L. (2004). Strain field fluctuation effects on lattice thermal conductivity of ZrNiSn-based thermoelectric compounds. *Applied Physics Letters*, *85*(7), 1140–1142. https://doi.org/10.1063/1.1783022

Yin, Y., Tudu, B., & Tiwari, A. (2017). Recent advances in oxide thermoelectric materials and modules. *Vacuum*, *146*, 356–374. https://doi.org/https://doi.org/10.1016/j.vacuum.2017.04.015

Yu, B., Liu, W., Chen, S., Wang, H., Wang, H., Chen, G., & Ren, Z. (2012). Thermoelectric properties of copper selenide with ordered selenium layer and disordered copper layer. *Nano Energy*, *1*(3), 472–478. https://doi.org/10.1016/j.nanoen.2012.02.010

Zhang, F., Niu, B., Zhang, K., Zhang, X., Lu, Q., & Zhang, J. (2013). Effects of praseodymium doping on thermoelectric transport properties of CaMnO3compound system. *Journal of Rare Earths*, *31*(9), 885–890. https://doi.org/10.1016/S1002-0721(12)60374-3

Zhang, F. P., Lu, Q. M., Zhang, X., & Zhang, J. X. (2011). First principle investigation of

electronic structure of CaMnO3thermoelectric compound oxide. *Journal of Alloys and Compounds*, *509*(2), 542–545. https://doi.org/10.1016/j.jallcom.2010.09.102

Zhang, F. P., Zhang, X., Lu, Q. M., Zhang, J. X., & Liu, Y. Q. (2011). Electronic structure and thermal properties of doped CaMnO3systems. *Journal of Alloys and Compounds*, *509*(10), 4171–4175. https://doi.org/10.1016/j.jallcom.2011.01.032

Zhang, J., Liu, R., Cheng, N., Zhang, Y., Yang, J., Uher, C., … Zhang, W. (2014). High-performance pseudocubic thermoelectric materials from non-cubic chalcopyrite compounds. *Advanced Materials*, *26*(23), 3848–3853. https://doi.org/10.1002/adma.201400058

Zhang, X. H., Li, J. C., Du, Y. L., Wang, F. N., Liu, H. Z., Zhu, Y. H., … Mei, L. M. (2015). Thermoelectric properties of a-site substituted lanthanide Ca0.75R0.25MnO3. *Journal of Alloys and Compounds*, *634*, 1–5. https://doi.org/10.1016/j.jallcom.2015.02.074

Zhang, X., & Zhao, L. D. (2015). Thermoelectric materials: Energy conversion between heat and electricity. *Journal of Materiomics*, *1*(2), 92–105. https://doi.org/10.1016/j.jmat.2015.01.001

Zhang, Y., Tao, R., Dong, W., Deng, Z., & Fang, X. (2009). Wide band-response laser-induced thermoelectric voltage in tilted orientation SrTiO3 single-crystal coated by La0.7Sr0.3CoO3 layer. *Optics and Laser Technology*, *41*(8), 968–971. https://doi.org/10.1016/j.optlastec.2009.04.006

Zhao, L.-D., He, J., Berardan, D., Lin, Y., Li, J.-F., Nan, C.-W., & Dragoe, N. (2014). BiCuSeO oxyselenides: new promising thermoelectric materials. *Energy & Environmental Science*, *7*(9), 2900–2924. https://doi.org/10.1039/C4EE00997E

Zhao, L. D., Dravid, V. P., & Kanatzidis, M. G. (2014). The panoscopic approach to high performance thermoelectrics. *Energy and Environmental Science*, *7*(1), 251–268. https://doi.org/10.1039/c3ee43099e

Zhao, L. D., Lo, S. H., Zhang, Y., Sun, H., Tan, G., Uher, C., … Kanatzidis, M. G. (2014). Ultralow thermal conductivity and high thermoelectric figure of merit in SnSe crystals. *Nature*, *508*(7496), 373–377. https://doi.org/10.1038/nature13184

Zhao, X. B., Ji, X. H., Zhang, Y. H., Zhu, T. J., Tu, J. P., & Zhang, X. B. (2005). Bismuth telluride nanotubes and the effects on the thermoelectric properties of nanotube-containing nanocomposites. *Applied Physics Letters*, *86*(6), 1–3. https://doi.org/10.1063/1.1863440

Zhong, B., Zhang, Y., Li, W., Chen, Z., Cui, J., Li, W., … He, Q. (2014). High superionic conduction arising from aligned large lamellae and large figure of merit in bulk Cu1.94Al0.02Se. *Applied Physics Letters*, *105*(12), 123902. https://doi.org/10.1063/1.4896520

Zhou, M., Li, J. F., & Kita, T. (2008). Nanostructured AgPbmSbTem+2 system bulk materials with enhanced thermoelectric performance. *Journal of the American Chemical Society*, *130*(13), 4527–4532. https://doi.org/10.1021/ja7110652

Zhu, Y. H., Su, W. Bin, Liu, J., Zhou, Y. C., Li, J., Zhang, X., … Wang, C. L. (2015). Effects of Dy and Yb co-doping on thermoelectric properties of CaMnO3ceramics. *Ceramics International*, *41*(1), 1535–1539. https://doi.org/10.1016/j.ceramint.2014.09.089